Astronomy & Astrophysics manuscript no. Galiullin_Gilfanov
January 18, 2022

Populations of super-soft X–ray sources in galaxies of different morphological types

I. Galiullin[1,2] and M. Gilfanov[1,3]

[1] Max Planck Institute for Astrophysics, Karl-Schwarzchild-Str.1, Garching b. Munchen D-85741, Germany e-mail: ilkham@MPA-Garching.MPG.DE
[2] Kazan Federal University, Kremlevskaya Str.18, 420008, Kazan, Russia
[3] Space Research Institute of Russian Academy of Sciences, Profsoyuznaya 84/32, 117997 Moscow, Russia

Received 24 September 2020; Accepted 30 November 2020

ABSTRACT

Aims. We study populations of soft and super-soft X-ray sources in nearby galaxies of various morphological types with the special emphasis on characterizing populations of stable nuclear burning accreting WDs.
Methods. Analysing the content of Chandra archive we assembled a sample of nearby galaxies suitable for studying populations of super-soft X-ray sources. Our sample includes 4 spiral galaxies, 2 lenticular galaxies and 3 ellipticals with stellar mass exceeding 10^{10} $M_\odot$ and X-ray sensitivity of the order of a few $\times 10^{36}$ erg/s. We used combination of hardness ratio and median energy to pre-select X-ray sources with soft spectra, and temperature – X-ray luminosity diagram to identify super-soft X-ray sources – likely nuclear burning accreting white dwarfs.
Results. For spiral galaxies, there is a distinct and rare population of super-soft sources, largely detached from the rest of sources on the $kT_{bb} - L_X$ plane. The boundary between these sources and the much more numerous population of harder (but still soft) sources is consistent with the boundary of stable hydrogen burning on the white dwarf surface. Combined spectrum of soft sources located outside this boundary, shows clear emission lines of Mg and S, which equivalent width is similar to that in the combined spectrum of a large number of confirmed supernova remnants in M83. This confirms earlier suggestions that the vast majority of so called quasi-soft sources are supernova remnants. In early-type galaxies, populations of super-soft sources are about a factor of ≈ 8 less abundant, in broad agreement with the population synthesis calculations. Specific frequencies of super-soft sources are: $(2.08\pm0.46)\times10^{-10}$ $M_\odot^{-1}$ in spiral galaxies and $(2.47\pm1.34)\times10^{-11}$ $M_\odot^{-1}$ in lenticular and elliptical galaxies, with the ratio of the latter to the former of 0.12 ± 0.05.

Key words. galaxies: individual — X-rays: binaries — stars: white dwarfs

1. Introduction

CAL 83 and CAL 87 – the two prototypical super-soft X-ray sources were discovered by Einstein observatory in the course of a survey of the Large Magellanic Clouds (Long et al. 1981). About a decade later, the first light observations of central region of LMC with ROSAT observatory led to a discovery of a similar source with a very soft spectrum, RX J0527.8-6954 (Trümper et al. 1991). With advent of Chandra and XMM-Newton, such sources were found in other, more distant, galaxies. Spectra of these sources are very soft and do not extend beyond $\sim 1-2$ keV, their approximation with the black body model giving temperatures of the order of $\sim 10-100$ eV and bolometric luminosities in the $\sim 10^{36}-10^{38}$ erg/s range (Greiner et al. 1991; Kahabka et al. 1994). It is the extreme softness of their spectra that gave rise to their name "super-soft X-ray sources" (SSS). Binary nature of some of these sources (CAL 83 and CAL 87 in the first place) was determined soon after their discovery (Pakull et al. 1988; Smale et al. 1988; Cowley et al. 1990) and, although they were initially thought to be low-mass X-ray binaries, it was soon realised that the compact object in these binaries is a white dwarf rather than a neutron star or a black hole (van den Heuvel et al. 1992). The proposition that the main source of energy in super-soft X-ray sources is thermonuclear burning of the accreted hydrogen naturally explained the unusual softness of their X-ray spectra, the combination of the energy output expected in hydrogen fusion and the surface area of a typical WD giving the effective temperatures in the correct range, close to the observed values (van den Heuvel et al. 1992).

Details of thermonuclear burning on the white dwarf surface are still a matter of debate. Calculations by Nomoto et al. (2007); Wolf et al. (2013) (and references therein) find that hydrogen fusion may proceed in a steady manner above some value of the mass accretion rate, in the so called stability strip stretching around $\dot{M} \sim$ few $\times 10^{-7}$ $M_\odot$ yr^{-1}, its exact location depending on the WD mass. In this regime classical steady SSS are observed, while at lower mass accretion rates hydrogen fusion on the WD surface is unstable, giving rise to the explosions of Classical and recurrent novae. On the other hand, calculations by Prialnik & Kovetz (1995); Yaron et al. (2005); Starrfield et al. (2013), suggest that nuclear burning is unstable at any mass accretion rate. Although the nova explosion itself is primarily observed in the optical band, nuclear burning of the residual hydrogen on the WD surface after the explosion generates soft X-ray emission and the system is observed as a post-nova super-

soft X-ray source (Truran & Glasner 1995; Wolf et al. 2013; Soraisam et al. 2016). Thus, existence of super-soft X-ray sources, steady or not, is envisaged in either scenario.

Although accreting WDs are interesting objects on their own right, they became of broader astrophysical importance as possible progenitors of type Ia supernovae (e.g. Whelan & Iben 1973; Nomoto 1982). However, before exploding as a supernovae, a white dwarf needs to increase its mass from the initial value, typically in the $\sim 0.5 - 1.0$ $M_\odot$ range, to near the Chandrasekhar mass limit of about ~ 1.4 $M_\odot$. For an accreting white dwarf, the only way to increase its mass is hydrogen and/or helium fusion on its surface. The mass growth is most efficient when nuclear burning is stable, as in all other regimes it is counteracted by various mass loss processes. However, growth of the white dwarf mass is also possible in certain domains of the parameter space, when the burning is unstable (Starrfield et al. 2013; Hillman et al. 2015). Nevertheless, it was demonstrated that the number of super-soft X-ray sources (Di Stefano 2010) and their total luminosity in the X-ray (Gilfanov & Bogdán 2010; Bogdán & Gilfanov 2011) and UV (Woods & Gilfanov 2013; Johansson et al. 2014; Woods & Gilfanov 2014) bands in nearby galaxies is by far insufficient to explain the observed SN Ia rates.

There is still no complete understanding of how population of nuclear burning accreting white dwarfs is related to the fundamental properties of their host galaxies, such as their stellar mass, star-formation rate and star-formation history and metallicity. On the theoretical side, there have been several attempts to address this problem by means of the population synthesis calculations (e.g. Yungelson & Livio 1998; Yungelson 2010). Recently, Chen et al. (2014, 2015, 2016) implemented a hybrid population synthesis calculations using the MESA code (Paxton et al. 2011, 2013) to compute the mass transfer phase of the binary evolution. They have produced a model which was in a reasonable agreement with a number of existing constrains on the soft X-ray luminosities and average intensity of ionising radiation field, as well as with statistics of classical novae in nearby galaxies.

Observational studies of SSS populations are often impeded by the extreme softness of their spectra, making their search and characterisation difficult. Nevertheless, there have been a number of successful attempts, which intensified with the advent of Chandra and XMM-Newton (e.g. Swartz et al. 2002; Di Stefano & Kong 2003, 2004; Pietsch et al. 2005; Henze et al. 2010, 2011, 2014). It was suggested that observed number of SSS on various types of galaxies are different (e.g. Di Stefano 2010). Bogdán & Gilfanov (2011) showed that specific frequencies of SSS with $L_X > 10^{36}$ erg/s in disks of late-type galaxies by factor of ~2 exceed that of bulges.

In this paper we continue the observational line of investigation of populations of accreting white dwarfs. To this end, we attempted to construct a suitable sample of galaxies from Chandra archive for search SSSs and implemented efficient source classification algorithms. Our goal is to identify steady nuclear burning white dwarfs and to estimate their specific frequencies in early- and late- type galaxies.

The paper is structured as follows: In Section 2 we introduce our sample of nearby galaxies observed by Chandra. Observations and data reduction procedures are described in Section 3. In Section 4 we introduce the initial source classification procedure based on combination of median energy and hardness ratio and in Section 5 we investigate properties of soft X-ray sources and separate nuclear burning white dwarfs from the rest of source population with the help of the temperature-luminosity diagram. The nature of soft and super-soft X-ray sources is described in Section 6 where we also estimate their specific frequencies and compare our results with previous work, and in Section 7 we summarise our findings.

2. A sample of nearby galaxies

Galaxies for the analysis were selected from Chandra observatory archive for cycles 1–20. To this end we selected observations from the following categories: normal galaxies, active galaxies and quasars, clusters of galaxies, galactic diffuse emission and surveys. Only archival observations with ACIS detector without grating were selected. For each galaxy, we grouped observations made within same Chandra cycle and selected the group having largest total exposure time. We then cross-matched aim-point positions of selected *Chandra* observations with positions of galaxies in RC3 catalogue (de Vaucouleurs et al. 1991) to select potentially interesting observations. For each galaxy, we used the match radius of $0.5{\times}D_{25}$. Parameters of galaxies required for the further selection were computed as follows. Stellar masses were computed from K_s band luminosities using mass-to-light ratios computed following the prescription of Bell & de Jong (2001). Classification of galaxies, distances and K_s-band magnitudes were taken from HyperLeda[1] catalogue (Makarov et al. 2014) and Updated Nearby Galaxy Catalog (Karachentsev et al. 2013). Absorption corrected $(B\text{-}V)_0$ colours were taken from RC3 catalogue.

2.1. Selection criteria

We built our selection procedure based on the following considerations.

i) Stellar mass of the host galaxy. Population synthesis calculations of Chen et al. (2014, 2015) predict specific frequencies of observable (apparent luminosity $L_X > 10^{36}$ erg/s) stable burning accreting WDs in spiral galaxies after 10 Gyrs of evolution at the level of $\sim 4\times10^{-10}$ ($\sim 2\times10^{-9}$) sources per $M_\odot$, assuming absorbing column density of 3×10^{21} (3×10^{20}) cm^{-2}. For elliptical galaxies their prediction is $\sim 10^{-10}$ sources per $M_\odot$ for hydrogen column density 3×10^{20} cm^{-2}. Based on these predictions we will be only considering sufficiently massive galaxies with stellar masses $M_* \gtrsim 10^{10}$ $M_\odot$, in which we can expect to find $\gtrsim 1$ nuclear burning accreting WD.

ii) Distance. We excluded from our analysis a few large nearby galaxies which do not fit, by a large margin, in the Chandra field of view and require analysing mosaics of a large number of observations. These are: Magellanic Clouds, M31 and M33. We should also exclude too distant galaxies which will suffer from confusion. However, they are automatically excluded based on the sensitivity arguments (item iv below)

iii) Inclination angle. Source populations in spiral galaxies which are viewed close to edge-on will be obscured by large intrinsic absorption by gas and dust in the disk, essentially reducing the numbers of expected super-soft sources to zero. Therefore in selecting late-type galaxies we applied

[1] http://leda.univ-lyon1.fr/

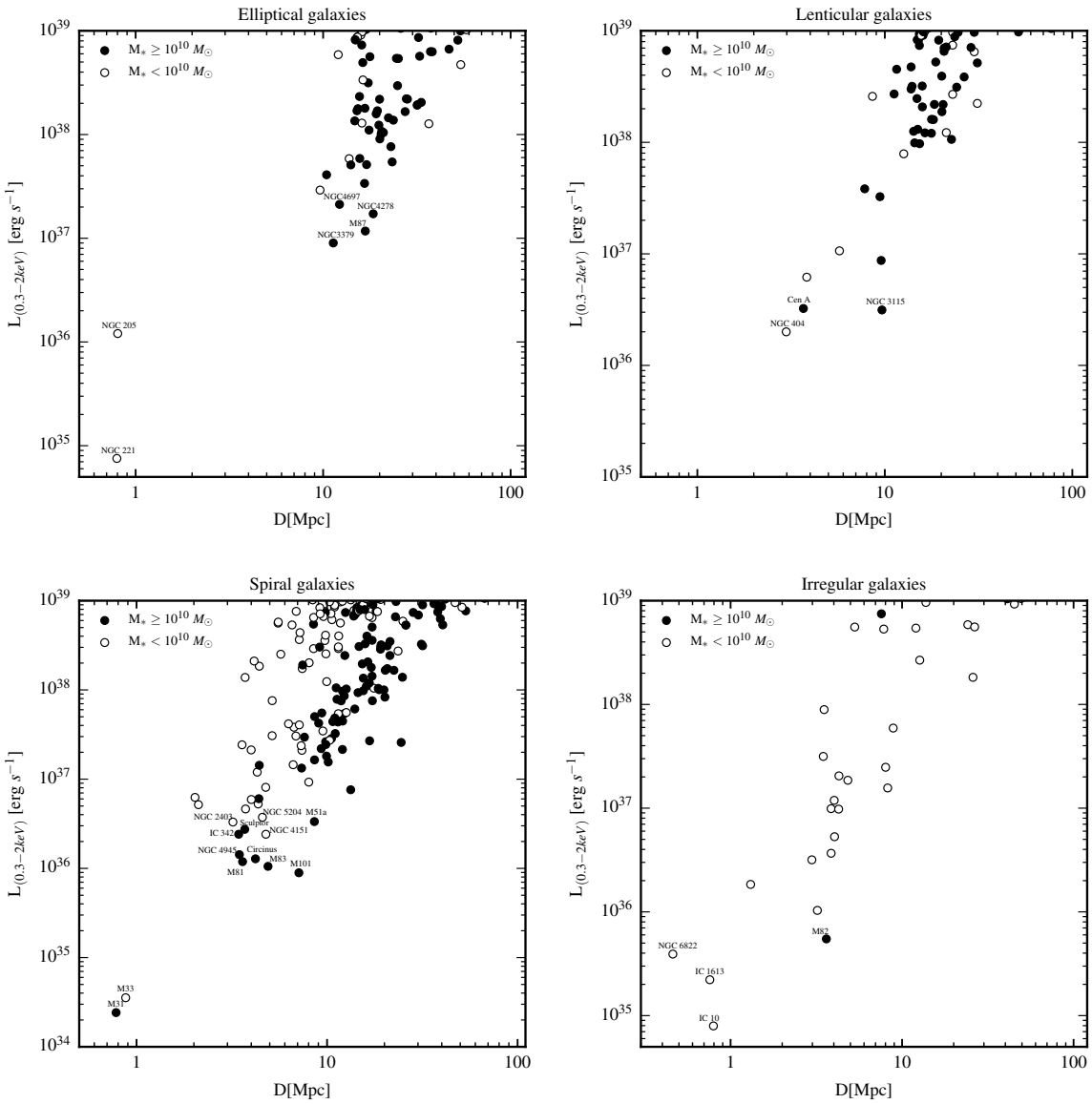

Fig. 1. The X-ray sensitivity–distance diagram of nearby galaxies observed by *Chandra* up to cycle 20. Each panel corresponds to a certain morphological type of galaxies. Filled (open) symbols correspond to galaxies with stellar mass $M_* \geq 10^{10}\ M_\odot$ ($M_* < 10^{10}\ M_\odot$). See Section 2 for details.

a criterion $i < 70$ degrees. For this reason, for example, Sculptor and NGC 4945 were not included in our final sample. No inclination cut was applied to early-type galaxies.

iv) Sensitivity limit of available archival data. The sensitivity limit of archival data can be estimated as follows:

$$L_X \approx 4\pi D^2 \times ECF \times \frac{S}{t}, \quad (1)$$

where D is distance to the galaxy, ECF is counts-to-ergs conversion factor, S is the limiting number of source counts required to detect and characterise a source, t is total exposure time of archival data. We assumed black body model with temperature 60 eV and require $S = 20$ counts to detect and classify a source. For each galaxy we obtained ECF from black body model ($kT = 60$ eV) modified by the Galactic absorption column density in the direction of the galaxy. For the latter we used the HI4PI data (HI4PI Collaboration et al. 2016). For cycles 7–20, in computing ECF, we used the ACIS detector aim-point response files from *Chandra* Calibration Database[2]. For cycles 1–6 we generated aim-point response files ourselves. Circinus (5.3×10^{21} cm^{-2}) and IC 342 (3.6×10^{21} cm^{-2}) galaxies with high Galactic absorption column densities were excluded from our sample. We also excluded M87 and M82 due to the presence of bright and complex diffuse emission in these galaxies.

We plot the distribution of galaxies of various morphological types on the distance – sensitivity limit plane in Fig.1. Based on these data we selected spiral galaxies M51, M81, M83, M101, lenticular galaxies Cen A and NGC3115 and elliptical galaxies NGC 3379, 4278 and 4697. For elliptical galaxies, sensitivity limits of the archival Chandra data exceed 10^{37} erg/s, this is however compensated by zero intrinsic absorption in these galaxies, see Section 5.2.

We experimented with the selection criteria in order to check if our sample can be improved by adding a few galaxies lying on the boundary of our luminosity and stellar mass selection. We found, however, that relaxing the sensitiv-

[2] ftp://cxc.cfa.harvard.edu/pub/caldb/

Table 1. List of nearby galaxies used to study populations of soft and super-soft X-ray sources.

Name	Type	D	Angular size	$(B–V)_0$	M_*	$N_{H,Gal}$	SFR
		(Mpc)	($D_{25} \times d_{25}$; PA)	RC3	(10^{10} $M_\odot$)	(10^{20} cm^{-2})	($M_\odot$/yr)
(1)	(2)	(3)	(4)	(5)	(6)	(7)	(8)
NGC 5236 (M83)	Sc	4.6	12.9′ × 11.5′; 54°	0.61	3.0	4.12	3.1
NGC 5194 (M51)	SABb	7.6	11.2′ × 6.9′; 173°	0.53	4.5	3.33	2.9
NGC 5457 (M101)	SABc	6.7	28.8′ × 26.9′; 36°	0.44	2.3	8.58	2.9
NGC 3031 (M81)	Sab	3.6	26.9′ × 14.1′; 157°	0.82	5.4	10.2	0.5
NGC 5128 (Cen A)	S0	3.4	25.7′ × 20.0′; 35°	0.88	4.9	2.35	0.8
NGC 3115	E-S0	9.7	7.2′ × 2.5′; 40°	0.94	6.9	3.88	–
NGC 3379	E	10.6	5.4′ × 4.8′; 71°	0.94	5.8	2.65	–
NGC 4278	E	16.1	4.1′ × 3.8′; 22.7°	0.90	6.0	2.04	–
NGC 4697	E	11.7	7.2′ × 4.7′; 70°	0.89	6.0	2.08	–

Notes: (1) – Galaxy name. (2) – Morphological type from HyperLeda catalogue (Makarov et al. 2014). (3) – Distances to galaxies obtained by the following methods: Cepheids: M83 (Saha et al. 2006), M81 and M101 (Freedman et al. 2001), Cen A (Ferrarese et al. 2007); planetary nebulae luminosity function: M51 (Ciardullo et al. 2002); surface brightness fluctuations: NGC 3379, NGC 3115, NGC 4278, NGC 4697 (Tonry et al. 2001). (4) – Major D_{25}, minor d_{25} diameters and position angles PA from RC3 catalogue (de Vaucouleurs et al. 1991). For several galaxies PA were adopted from elsewhere: M83 (Ho et al. 2011); M51 (Colombo et al. 2014); M101 (Hu et al. 2018); NGC 3379 and NGC 4278 (Peletier et al. 1990). (5) – The total colour indexes corrected for galactic and internal extinction from RC3 catalogue. (6) – Stellar mass within D_{25} of the galaxy obtained by mass-to-light ratio for K_s band with colour index $(B–V)_0$ from RC3 using calibration from Bell & de Jong (2001). Total K_s magnitudes were calculated using data from 2MASS Large Galaxy Atlas (Jarrett et al. 2003). Absolute K_s magnitude of the Sun was assumed to be $K_{s,\odot}$=3.27 (Willmer 2018). (7) – Galactic absorption column densities (HI4PI Collaboration et al. 2016). (8) – Star formation rates of spiral galaxies were adopted from Jarrett et al. (2013), for Centaurus A from Espada et al. (2019). Values were corrected to the distance given in column (3).

ity threshold we need to raise the luminosity cut on the $kT_{bb} - L_X$ plane (Section 5.2) which actually leads to the loss of super-soft sources of lower luminosity and degradation of the statistical accuracy of our analysis. Adding less massive galaxies, below the assumed cut of 10^{10} $M_\odot$, on the other hand, does not lead to the quick improvement of the sensitivity to the populations of SSS as the total mass already included in the analysis exceeds $\approx 4 \times 10^{11}$ $M_\odot$. We therefore conclude that the list of galaxies assembled here is reasonably optimal for the current analysis. Basic parameters of these galaxies are summarised in Table 1.

3. Observations and Data Reduction

The observations were processed by following a standard CIAO (Fruscione et al. 2006) threads[3] (CIAO version 4.8 and CALDB version 4.7.1). We used tool *chandra_repro* to reprocess data and create level 2 event file. To improve absolute astrometry we used *wcs_match* and *wcs_update*. Astrometry correction was done relative to the observation with the longest exposure time using positions of bright X-ray sources to match frames. Event files have been merged by *reproject_obs* with aim point position of observation with the longest exposure taken as the reference. Combined images and exposure maps were obtained running *flux_obs*. In Table 2 we present short information about observations used in analysis. Detail information available in Appendix A.

3.1. Source detection

Source detection was performed with *wavdetect* tool. We chose to use small $\sqrt{2}$ scale series with power of 0–3 of the wavelet functions to minimize the spurious detections associated with soft diffuse emission in galaxies. Scales of wavelets correspond to variation of the point spread function (PSF) within an aim point of single ACIS chip. We set up following parameters of *wavdetect* to create a background map from merged image: *bkgsigthresh*=0.01, *maxiter* = 10, *iterstop* = 10^{-6}. The false source detection probability threshold was chosen at 10^{-7}. Mask filtering were applied to all images of galaxies using exposure maps. Pixels were included to the source detection region where exposure map values were greater than 20% of the maximum (*expthresh* =0.2). False colour X-ray images of all galaxies with their D_{25} and source detection regions are presented in Appendix B.

To maximise sensitivity of source detection, we used combination of the following energy bands: 0.3–1 keV; 1–2 keV; 0.3–2 keV; 0.5–8 keV; 2–8 keV bands. We ran *wavdetect* in each of these bands and merged their results into a single source list, excluding duplications. To this end we used STILTS package (Taylor 2006), with the match radius equal to the sum of their PSFs radii defined at the

[3] http://cxc.harvard.edu/ciao/index.html

Table 2. Properties of galaxies and statistics of their X–ray source populations.

Name	Date	Cycle	#	Exposure (ksec)	$L^{faint}_{0.3-2}$ (10^{35} erg/s)	N_{src}	N^{soft}_{src}	N^{SSS}_{src}	M_* ($10^{10} M_\odot$)
(1)	(2)	(3)	(4)	(5)	(6)	(7)	(8)	(9)	(10)
NGC 5236 (M83)	23/12/2010 - 28/12/2011	12	10	729.63	3.0	276	116	14	2.5
NGC 5194 (M51)	09/09/2012 - 10/10/2012	13	7	745.33	5.8	245	105	5	4.1
NGC 5457 (M101)	19/01/2004 - 01/01/2005	5	24	952.01	6.3	221	89	11	2.0
NGC 3031 (M81)	26/05/2005 - 06/07/2005	6	15	175.92	3.5	161	50	2	5.3
NGC 5128 (Cen A)	22/03/2007 - 30/05/2007	8	6	561.72	11.7	286	88	2	3.6
NGC 3379	23/01/2006 - 10/01/2007	7	4	305.53	20.1	87	30	1	5.8
NGC 3115	18/01/2012 - 06/04/2012	13	8	985.40	7.7	136	32	0	6.9
NGC 4278	16/03/2006 - 20/04/2007	7	5	433.30	36.0	244	92	2	6.0
NGC 4697	26/12/2003 - 18/08/2004	5	4	153.70	34.7	102	38	2	6.0

Notes: (1) – Galaxy name. (2) – Time interval of observations. (3) – *Chandra* cycle during which most of observations were made. (4) and (5) – Total number of observations and their exposure time. Full information about archival data used in this work are available in Appendix A. (6) – X-ray luminosity of faintest source detected in combined data. In computing this luminosity absorbed black body model was used with temperature $kT = 60$ eV and absorption column density computed as described in Section 5.1. (7) – Total number of detected sources (see Section 3.1). (8) – Total number of sources classified as soft according to the method described in Section 4, and having ≥ 20 net counts. (9) – Number of super-soft X-ray sources – sources located to the left of the stable hydrogen burning boundary in Fig.5 (see Section 6.1 and Appendix C.1). (10) – Stellar mass within the spatial region used for source detection.

80% encircled fraction. In the final merged list we chose coordinates of sources in the band where the significance of detection was maximal. In the very inner regions of some galaxies *wavdetect* found multiple overlapping sources. Visual inspection of the images showed that many of these sources are likely false detections caused by presence of substructures in the bright and complex diffuse emission of the nucleus. In many cases it appears impossible to separate true compact sources from such false detections. For this reason we decided to exclude in M51, M83 and Centaurus A galaxies their central regions of radius of 15″. In the case of Centaurus A we also excluded regions around bright X-ray jets similar to Voss & Gilfanov (2006).

To define source and background counts extraction regions we produced PSF maps. In order to account for PSF variations across the combined image, we created PSF map for each observation with *mkpsfmap* tool using encircled energy of 80%, and combined individual maps weighting them with respective exposure maps. Combined source spectra used in the further analysis were extracted using CIAO tool *specextract*. For source regions we used circles with the radius equal to the 80% PSFs radius from the exposure-weighted PSF map. The background regions were defined as annuli with the inner and outer radii equal to two and four times the PSFs radius respectively. The source count rates were corrected for the source counts leakage to the background region. When source or background regions of different sources overlapped, we excluded overlapping parts from the counts summation, correcting the PSF fractions accordingly.

The lists of detected sources were analysed to identify spurious detection due to fluctuations of local background. For each sources we tested the null hypothesis that observed counts in source and background regions are Poissonian realizations of local background with the same mean (Weisskopf et al. 2007, see Appendix A). We estimated probabilities using source and background counts from merged images in 0.3–2 keV band. All detections of statistical confidence of less than 3σ were excluded from the final source list. Additionally, an eye inspection of X-ray images has not revealed any potential spurious detections. In Table 2 we summarise numbers of X-ray sources detected in galaxies of our sample.

3.2. Stellar masses of the final sample of galaxies

Stellar masses of galaxies within D_{25} and within the source detection regions listed in Tables 1 and 2 were determined following prescription of Zhang et al. (2012) as summarised below. We used background subtracted images from 2MASS Large Galaxy Atlas (Jarrett et al. 2003). Bright sources were visually removed from the images. Net counts of the images S were converted into magnitude using zero-point magnitude KMAGZP from a headers of fits files.

$$m_{\rm K} = {\rm KMAGZP} - 2.5\ \log({\rm S}) \quad (2)$$

We obtained K_s band absolute magnitudes using distances listed in Table 1. In computing luminosities, Solar absolute magnitude in K_s band was assumed to be $K_{s,\odot}$=3.27 (Willmer 2018). Final stellar masses of the galaxies were obtained using K_s band mass-to-light ratio (Bell & de Jong 2001).

$$\log(M_*/L_{\rm K}) = -0.692 + 0.652(B-V)_0, \quad (3)$$

where $L_{\rm K}$ is K_s band luminosity and $(B\text{-}V)_0$ is colour index corrected for galactic and internal extinction (see Table 1).

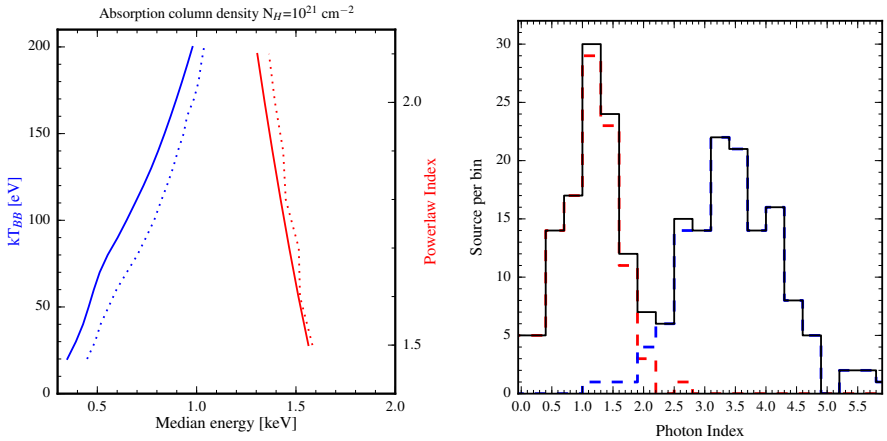

Fig. 2. *Left*: Relation of the median energy to the temperature of a black body model (left-hand curves and y-axis, blue in the color version of this plot) and to the photon index of a power law model (right curves and y-axis, red). Simulations for Chandra ACIS-S detector with Cycle 13 (2012) response. Absorption column density of 10^{21} cm^{-2} was assumed. *Solid lines* show to models without background, *dotted lines* – models with 50% contribution of background counts. Parameter ranges are relevant to super-soft sources and X-ray binaries, and the two types of spectra are clearly separated at about $\tilde{E} \approx 1.0 - 1.3$ keV. *Right*: Verification of the source classification procedure in M51. Distribution of sources having median energy $\tilde{E} \leq 2$ keV over photon index of power law model. *The blue and red dashed* histograms show distributions of sources classified as soft and hard, the *black solid line* is the total distribution. Bi-modality of the distribution of sources over photon index is obvious.

4. Source classification

4.1. The method

To classify and to separate soft and super-soft sources from sources with more usual spectra we used combination of hardness ratio HR and median energy $\tilde{E}$. The hardness ratio was defined as a ratio of the hard band count rate to the total broad band count rate:

$$HR = \frac{R(2-8\ keV)}{R(0.3-8\ keV)}\ , \tag{4}$$

where R is the background subtracted count rate in the respective energy band. Statistical error of the hardness ratio was calculated using standard error propagation.

Median energy $\tilde{E}$ for each source was calculated from its observed counts spectrum considering the 0.3–8.0 keV energy band. The statistical error was computed using the standard formula for the variance of the sample median (Rider 1960) where the probability density at the median energy was approximately determined from observed counts distribution. In computing the median energy we chose not to subtract background from the source spectrum. Simulations have demonstrated that for the typical source and background spectra we are dealing with, this does not affect our source classification procedure (see Fig. 2 and its discussion below).

The motivation behind our choice of the parameters used for source classification is fairly obvious. The median energy characterizes overall softness of the spectrum. The Fig.2 (left panel) shows median energies of absorbed black body and power law models. Temperatures and photon index axes are located on the right and on the left side of Fig.2 (left panel). As one can see from the plot, in the parameter range relevant to nuclear-burning accreting white dwarfs ($kT \lesssim 200$ eV) and X-ray binaries/AGN/stars ($\Gamma \lesssim 2$), the two types of sources occupy different domains along the $\tilde{E}$ axis with some gap in between[4]. Therefore one may expect a bi-modal distribution of sources over $\tilde{E}$ (which may however be smeared by statistical uncertainties).

We used M51 to illustrate and verify classification of sources using their median energy (see corresponding panels in Fig.3). To this end we fit background subtracted spectra of all sources having $\tilde{E} \leq 2$ keV[5], with an absorbed power law model. The absorption column density for each source was fixed as described in Section 5.1 below. Distributions of soft and hard X-ray sources over photon index are shown in the right panel of Fig.2. From these distributions it is clear, that indeed, the sources classified as soft and hard occupy different domains along the photon index axis. Small overlap of the two distributions is caused by statistical uncertainties in measuring the median energy and photon index.

This comparison shows that a classification scheme based on the median energy is efficient in identifying sources with soft spectra. The hardness ratio, on the other hand, characterizes the presence of source emission above 2 keV and helps to identify sources having low $\tilde{E}$ but also featuring hard emission components extending to higher energies. Such hard spectral components are not typical for nuclear burning white dwarfs and may be encountered, for example, in accreting black holes in the soft state and in some of supernova remnants.

[4] Note that particular location of the boundary between super-soft sources and X-ray binaries in Fig.2 depends on the hydrogen column density N_H and details of the instrument response. The curves plotted in Fig.2 (left panel) have been computed for 2012 (Cycle 13) Chandra ACIS-S response. For other Chandra calibration epochs their shape and location along x-axis will be (slightly) different.

[5] Some of the hard sources are located at $\tilde{E} \gtrsim 2$ keV, too large for a power law spectrum with slope of $\Gamma \lesssim 2$ (Fig.2, left panel). These are either sources with genuinely large $\tilde{E}$, e.g. absorbed AGN, or faint sources where contribution of the instrumental background becomes important and shifts the median energy to non-physically large values.

Finally, we note that the median energy is not efficient in separating the bulk of SNRs from white dwarfs. This can be achieved with more detailed spectral fitting, which however produces meaningful results only for the brightest sources.

Use of the median energy and hardness ratio for characterization of the spectral shape is not entirely new in X-ray astronomy, for example Hong et al. (2004) proposed to use various quantiles and Prestwich et al. (2003) used color-color diagram for this purposes. Di Stefano & Kong (2003) used hardness ratio to classify super-soft X-ray sources in external galaxies. Color-color diagrams and hardness ratio techniques were used in numerous other work not mentioned here. However, to our knowledge, combination of the median energy and hardness ratio was employed for separating super-soft sources from the bulk of the population for the first time in this paper.

4.2. Distribution of sources in $HR - \tilde{E}$ plane

The distribution of sources on the hardness ratio – median energy plane is shown in Fig.3. In producing these plots we applied to all data sets cuts of 20 net counts in order to exclude sources with too large uncertainties. For each galaxy we also plot distribution of sources over the median energy.

4.2.1. Late-type galaxies

Distributions of the sources over median energy in M51, M83 and M101 are clearly bimodal. Their HR-$\tilde{E}$ diagrams have a distinct and relatively compact populations of soft sources at $\tilde{E} \lesssim 1$ keV and $HR \sim 0$ along with the more extended tail of sources with more usual harder spectra. Based on their distributions over the median energy we chose the boundary of $\tilde{E}_0 = 1.2$ keV to select soft sources in these galaxies. Hard sources were excluded from further consideration. We also excluded from further analysis sources having statistically significant flux ($\geq 3\sigma$) detected above 2 keV. Total numbers of so selected soft sources are presented in Table 2.

The median energy distribution of sources in M81 shows a single peak at $\tilde{E}_0 \approx 1.5$ keV. with a possible shoulder towards lower values of $\tilde{E}$. Lack of bi-modality may be a consequence of the star-formation history of this galaxy as discusses in section 6.4. Due to absence of obvious bimodality of the source distribution we applied selection criterion based on the absence of hard flux. In particular, we excluded from further analysis sources, having statistically significant flux ($\geq 3\sigma$) detected above 2 keV. Their numbers are listed in Table 2 .

4.2.2. Early-type galaxies

Distributions of sources over median energy for elliptical and lenticular galaxies is also uni-modal with the low energy shoulder present for some galaxies. Similar to M81, we kept only sources without statistically significant flux above 2 keV.

5. Observed properties of soft sources

5.1. Equivalent hydrogen column density

Due to the softness of sources under consideration, the value of equivalent hydrogen column density N_H is important for accurate spectral analysis. This problem is of relevance for late-type galaxies.

Because of degeneracy with other parameters N_H is difficult to determine from fitting X-ray spectra, especially for fainter sources with smaller number of counts, which constitute the majority of our sample. Therefore we chose to fix N_H at values determined in radio band. To this end we combined CO 2-1 and 21 cm maps from the HI Nearby Galaxy Survey (THINGS, Walter et al. 2008) and the HERA CO-Line Extragalactic Survey (HERACLES, Leroy et al. 2009). For each source we computed absorption column density as

$$N_{\rm H} = N_{\rm H,Gal} + f \times (N_{\rm HI} + 2 \times N_{\rm H_2}) \quad (5)$$

where $N_{\rm H,Gal}$ is the Galactic hydrogen column density in the direction of galaxy (HI4PI Collaboration et al. 2016), $N_{\rm HI}$ and $N_{\rm H_2}$ are column densities of neutral and molecular gas from THINGS and HERACLES surveys respectively, computed as follows:

$$N_{\rm HI}[{\rm cm}^{-2}] = \frac{1.11 \times 10^{24} \times {\rm I_{HI}}}{{\rm FWHM_{maj}}[''] \times {\rm FWHM_{min}}[''] } \quad (6)$$

where $\rm I_{HI}$ is velocity-integrated intensities of THINGS maps in units of Jy beam^{-1} km s^{-1}. $\rm FWHM_{maj}$ and $\rm FWHM_{min}$ are the major and minor axes of the beam in arsec (Walter et al. 2008, see Eq. 5). For $N_{\rm H_2}$ we used:

$$N_{\rm H_2}[{\rm cm}^{-2}] = \frac{\rm R_{21}}{0.8} \times {\rm X_{CO}} \times {\rm W_{CO}}, \quad (7)$$

where $\rm W_{CO}$ is HERACLES velocity-integrated CO J = 2 → 1 map intensity in units of K km s^{-1}, $\rm X_{CO}$ is the CO J = 1 → 0 to $\rm H_2$ conversion factor and $\rm R_{21}$ is CO J = 2 → 1 to CO J = 1 → 0 ratio. We assumed Galactic value of $\rm X_{CO}$ = 2×10^{20} cm^{-2} (K km s^{-1})$^{-1}$ (Strong & Mattox 1996; Dame et al. 2001) for majority of galaxies and $\rm R_{21}$=0.8 (see Leroy et al. 2009, Eq.3 and references therein).

The $\rm X_{CO}$ factor is known to vary between galaxies, in particular for M51 it is ∼ 4 times smaller than the Galactic value (Garcia-Burillo et al. 1993; Guelin et al. 1995). For M81, no CO maps of sufficient quality are available and we accounted only for absorption by neutral hydrogen. For M83 we used CO 1–0 intensity map from NED[6] where galaxy was observed by Crosthwaite et al. (2002) with NRAO 12m telescope.

Table 3 shows median values of absorption column densities $N_{\rm H}$ of soft sources in late-type of galaxies for two cases: $f = 0.5$ and $f = 1$. We adopted $f = 0.5$ i.e. that sources are subjected to a half of the absorption intrinsic to galaxy. Naively, this corresponds to the assumption that all sources are located close to the mid-plane of the host galaxy.

We analysed spectra of bright sources with ≥200 net counts and compared results of X-ray spectral fits with fixed N_H with spectral fits where N_H was a free parameter of the fit. The results are shown in Fig.4. As one can see, although

[6] NASA/IPAC Extragalactic Database: https://ned.ipac.caltech.edu

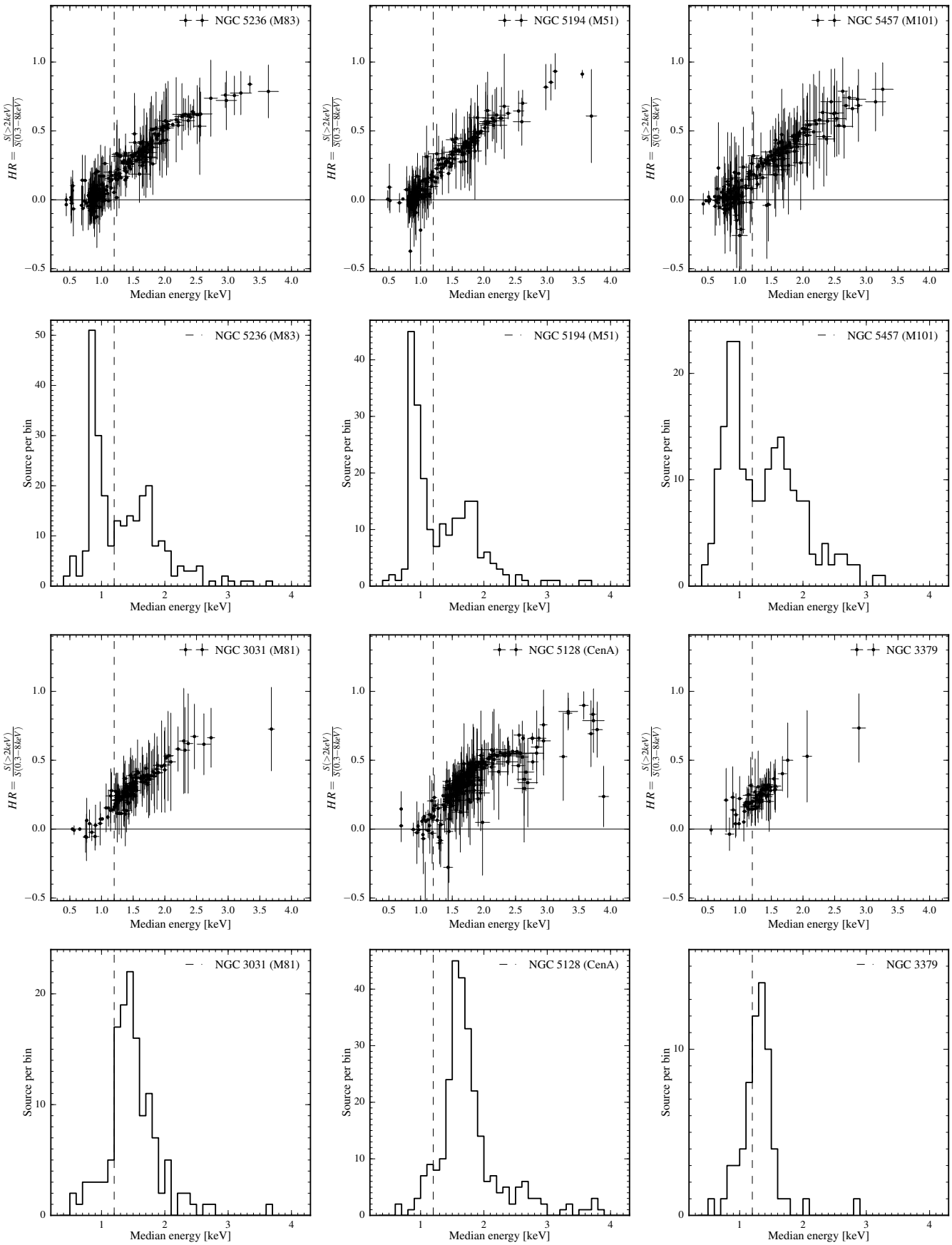

Fig. 3. – *continued*

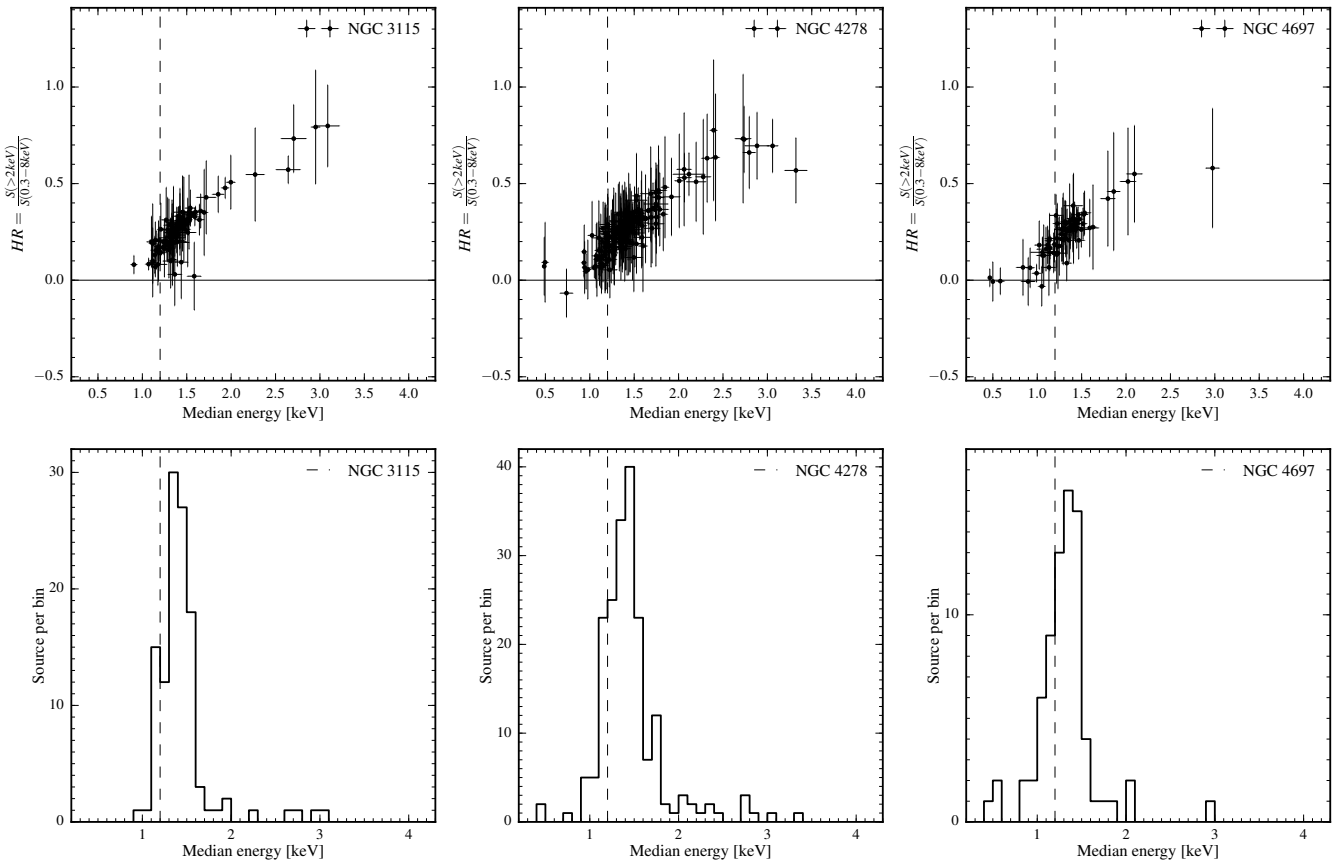

Fig. 3. Hardness ratio versus median energy diagram for compact X-ray sources in galaxies of our sample. Only sources with ≥ 20 net counts are plotted. Dashed lines show the median energy boundary of $\tilde{E}_0$ = 1.2 keV (see Section 4.2). Distributions of sources over the median energy are plotted below corresponding median energy – hardness ratio diagram.

Table 3. Absorption column densities for late-type galaxies.

Name	$N_{H,f=0.5}$	$N_{H,f=1}$	Metallicity	References
	(10^{21} cm^{-2})	(10^{21} cm^{-2})	($Z_\odot$)	for metallicity
(1)	(2)	(3)	(4)	(5)
NGC 5236 (M83)	3.35	6.35	~ 0.5*	Bresolin et al. (2009)
NGC 5194 (M51)	1.84	3.51	~ 0.7*	Moustakas et al. (2010, see Table 8,KK04 calibration)
NGC 3031 (M81)	1.30	1.53	~ 0.7*	Stanghellini et al. (2014)
NGC 5457 (M101)	1.67	2.46	1	Assumed for spectral fit

(1) – Galaxy name. (2) and (3) – Median value of N_H of soft sources calculated assuming $f = 0.5$ and $f = 1$ (eq.5) respectively. (4) – Metallicities of galaxies used in spectral fit and (5) – references for these values. Metallicities marked with (*) were recalculated relative to solar abundance $[O/H]_\odot = 4.9\times10^{-4}$ of Wilms et al. (2000).

there is a considerable scatter in the N_H values, values of temperature and, especially, X-ray luminosity are in a reasonable overall agreement. Unfortunately, such analysis is possible only for a small fraction of sources. We therefore chose to use fixed absorption column density, computed, for each source, from Eq.5.

Elliptical and lenticular galaxies in our sample have much lower intrinsic neutral hydrogen column density, below ~ few × 10^{19} cm^{-2} (Serra et al. 2012). We therefore can safely assume $N_H = N_{H,Gal}$ for early-type galaxies in our sample, with a caveat regarding Centaurus A. In the dust lanes of this galaxy, absorption column density is at the nearly constant level of ≈ 5×10^{21} cm^{-2} and drops rather sharply outside the dust lanes (Struve et al. 2010). Therefore, for the sources located in the dust lanes (about ~ 1/3 of all soft sources in Centaurus A) we accounted for the intrinsic absorption in the same way as it was done for spiral galaxies, but assuming a constant value of intrinsic absorption of 5×10^{21} cm^{-2}, while for the sources outside dust lanes we used Galactic value. We found that particu-

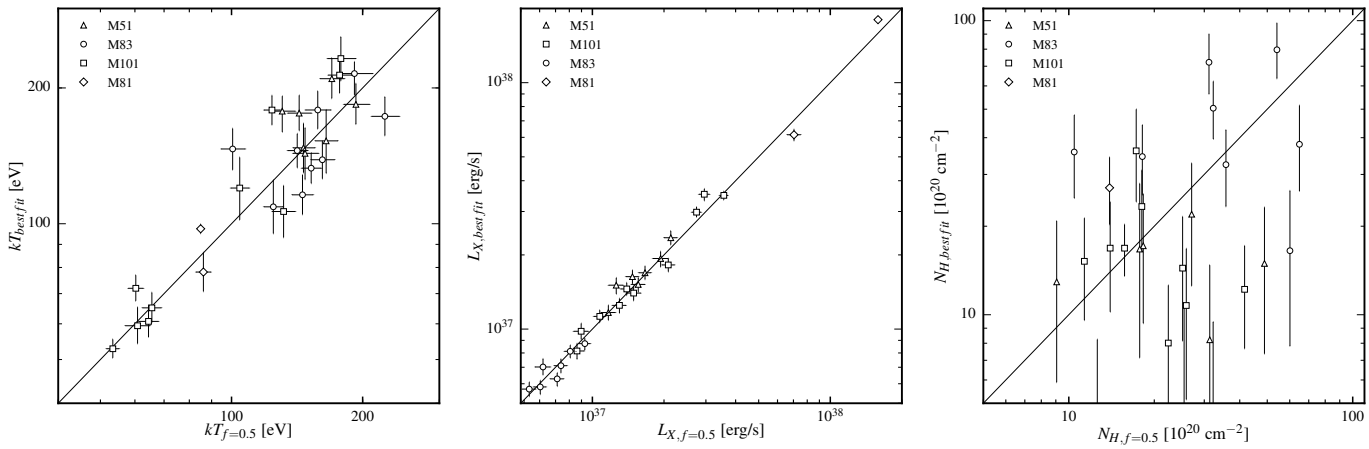

Fig. 4. Relations between black body temperature (left) and absorbed X-ray luminosity (centre) values computed with N_H being a free parameter of X-ray spectral fit (y-axes) and for N_H computed from Eq.5 with $f = 0.5$ (x-axes). The right hand panel shows relation between bets-fit N_H and N_H computed from Eq.5. Only sources with net counts ≥200 are shown. Errors are 1σ. See Section 5.1 for more details.

lar details of this calculation are unimportant. It should be also noted that Centaurus A galaxy also stands out in the early-type galaxy sample due to its ongoing star-formation on the level of $\sim 0.8\ M_\odot$/yr (Espada et al. 2019). It will be further discussed in Section 6.2.

5.2. X-ray spectral analysis and $kT_{bb} - L_X$ diagram

Spectra of X-ray sources, classified as soft, were approximated with an absorbed black body model, with the absorption column density being fixed at the values computed as described in Section 5.1. For spectra with small number of counts absorption correction of X-ray luminosity often bears large uncertainties and may lead to physically meaningless values. Therefore we chose to use absorbed X-ray luminosities of sources in further analysis and apply absorption to models, when comparing them to the data. We used Tuebingen-Boulder ISM absorption model (Wilms et al. 2000) (*tbvarabs* model in XSPEC). Abundances of late-type galaxies were fixed at values listed on Table 3. For early-type galaxies Wilms et al. (2000) solar elemental abundance was assumed. The spectral fit was performed with *XSPEC* (Arnaud 1996) in the 0.3–8 keV energy band using C – statistics (Cash 1979). Background spectrum was included in the spectral fitting. Spectra were binned to have at least one count per bin, following recommendations of the XSPEC manual[7]. Confidence intervals for the parameters were obtained using *error* command in XSPEC.

Distribution of sources on the X-ray luminosity – temperature (hereafter $kT_{\rm bb} - L_{\rm X}$) plane is shown in Fig. 5. In plotting $kT_{\rm bb} - L_{\rm X}$ diagram we applied a cut of 20 net counts, in order to exclude faint sources with too large error bars. The X-ray luminosities were computed for the 0.3–2 keV energy band. The thin solid line near the bottom of each panel shows X-ray luminosity corresponding to 20 net counts, as a function of the black body temperature. In plotting these curves we converted counts to rate using the maximal exposure time of the observation. The absorbed X-ray luminosity was computed using count rate – flux conversion for the black body spectrum with the given temperature and absorption column density. The luminosity corresponding to 20 counts exceeds by a factor of ∼3 luminosities of faintest sources, therefore samples of sources above these curves should not be subject to significant incompleteness effects.[8]

On each panel, the blue dashed line shows the luminosity limit for M51 data corrected for the difference between absorption column densities in M51 and the galaxy under consideration. The correction factor is close to unity at temperatures exceeding a few hundred eV. However, it may be considerable at low temperatures, for soft spectra. These lines permit to compare sensitivities of different datasets independently of the absorption. In particular, this comparison demonstrates that despite the rather significant scatter in Chandra exposure and distances to galaxies, selected galaxies have comparable detection sensitivity to sources with soft spectra.

In Fig.5, solid red curves show the lower bound of the stability strip for the nuclear burning of hydrogen on the WD surface (Wolf et al. 2013). In plotting these curves, we used the Stefan-Boltzmann law to compute the effective temperature and the mass-radius relation for zero-temperature white dwarfs from Panei et al. (2000). The WD mass changes along the curve from $0.51 M_\odot$ to $1.34 M_\odot$. We then used the black body model in XSPEC, apply ISM absorption and compute 0.3–2 keV band luminosity, corresponding to the given WD mass and effective temperature. For late-type galaxies, absorption column densities were fixed at corresponding median values from Table 3 while for early-type galaxies we used the Galactic value $N_{\rm H,Gal}$, as explained above. For Centaurus A we also show location of this boundary for sources located in the dust lanes. Green lines in Fig.5 show tracks of the spectral model of relativistic accretion disk around a Schwarzschild black hole (Ebisawa et al. 1991). Along these lines, the mass accretion rate

[7] https://heasarc.gsfc.nasa.gov/xanadu/xspec/manual/XSappendixStatistics.html

[8] See, for example, incompleteness function of Chandra data for Centaurus A in Voss & Gilfanov (2006). From their Fig A1, incompleteness effects become relatively small at luminosities $\sim 2-3$ larger than detection limit of the data.

changes from $0.02\dot{M}_{\rm Edd}$ to $\dot{M}_{\rm Edd}$, different lines correspond to the different black hole mass as marked by the number near the curves. To compute these tracks, we approximated the accretion disk emission spectrum by an absorbed black body model. The absorption was applied similar to other models plotted in the figure.

All sources plotted in Fig.5 have no significant ($\geq 3\sigma$) flux above 2 keV. For three late-type galaxies with bi-modal median energy distributions (M83, M51 and M101) we plot only sources with median energy $\tilde{E} \lesssim 1.2$ keV. These sources show rather compact distributions in the $kT_{\rm bb} - L_{\rm X}$ plane with temperatures 20~300 eV and X-ray luminosities in 10^{36}~10^{38} ergs/s range. For other galaxies, we only used the criterion of lack of statistically significant ($\geq 3\sigma$) emission above 2 keV. For these galaxies, distributions of sources extend significantly towards higher temperatures (cross-hair symbols in Fig.5), which is not surprising as such a selection includes many sources with regular spectra. These sources are dominated by X-ray binaries and background AGN and their discussion is beyond the scope of this paper. Sources with low median energy $\tilde{E} \lesssim 1.2$ keV (solid orange symbols) tend to have lower temperatures than the bulk of sources in these galaxies and will be discussed in the following section, along with soft sources in M83, M51 and M101.

5.3. Foreground stars

To identify foreground stars we cross-correlated the lists of soft X-ray sources with the GAIA (Gaia Collaboration et al. 2016) catalog, Data Release 2 (Gaia Collaboration et al. 2018). With the search radii of 2″ we typically found ~2 matches per galaxy except for Centaurus A galaxy where we found 12 matches. Large number of matches for Centaurus A is caused by its relative proximity to the Galactic plane. Some of the GAIA matches have statistically significant measurements of parallax or proper motion, with S/N>3. These sources are classified as stars in the Galaxy and excluded from further analysis. We mark them with open diamonds in Fig. 5.

6. Nature of soft and super-soft X-ray sources

Based on first Chandra studies of nearby galaxies it was proposed to divide soft sources in external galaxies into super-soft and quasi-soft (Di Stefano & Kong 2003, 2004). The former are characterised by color temperatures of $kT \lesssim 100$ eV and are believed to be mostly associated with accreting white dwarfs with nuclear burning of hydrogen on their surface, while the latter have temperatures in the range $kT \sim 100 - 300$ eV and, possibly, are unrelated to white dwarfs.

6.1. Super-soft X-ray sources and accreting white dwarfs

In the commonly used albeit (over)simplified picture, it is assumed that the spectral energy distribution of nuclear burning WDs can be roughly described by a black body spectrum (cf. Woods & Gilfanov 2013) with the color temperature close to the effective temperature. Observations of well-known super-soft X-rays sources in the Milky Way, Magellanic Clouds (e.g. Greiner 1996; Kahabka & Trumper 1996) seem to broadly support this assumption. The effective temperature of an accreting white dwarf powered by nuclear burning of hydrogen on its surface is given by:

$$T_{\rm eff} = \left(\frac{\epsilon_H X_H \dot{M}}{4\pi R_{\rm phot}^2 \sigma_{SB}}\right)^{1/4} = 67\left(\frac{\dot{M}}{5\times10^{-7}\ M_\odot/yr}\right)^{1/4}\left(\frac{R_{\rm phot}}{10^{-2}\ R_\odot}\right)^{-1/2}\ eV \quad (8)$$

where $\epsilon_H = 6\times10^{18}$ erg/g is the energy release in hydrogen fusion per unit mass of hydrogen, $X_H \approx 0.72$ is hydrogen mass fraction of the accreting material, $\dot{M}$ is the mass accretion rate and $R_{\rm phot}$ is the photospheric radius of the hydrogen burning layer. Numerical calculations show that at the bottom of the stability strip $R_{\rm phot} \sim R_{\rm WD}$ and photospheric radius increases with increase of $\dot{M}$ (Wolf et al. 2013).

The red solid line in Fig.5 shows the temperature–luminosity relation computed at the lower bound of the stability strip and assuming $R_{\rm phot} = R_{\rm WD}$. For the definition of the (white dwarf mass dependent) lower boundary of stable nuclear burning we used results of Wolf et al. (2013) and for the WD radius we used zero temperature radius (depending on the WD mass) from Panei et al. (2000). The region on the $kT_{bb} - L_X$ diagramm above and to the left of this line is permitted for accreting white dwarfs stably burning hydrogen on their surface, while in the part of the diagram to the bottom-right stable nuclear burning of hydrogen is not possible and it should be populated with other types of soft X-ray sources. Indeed, in Fig.5 one can see that in late-type galaxies (M83, M51, M101 and M81), there is a distinct group of rare soft and luminous sources located above these line. These sources have temperatures of ~several tens of eV and seem to clearly stand out in the populations of soft sources in these galaxies. In interpreting Fig.5 one should bear in mind that it shows absorbed luminosities in $0.3-2.0$ keV band and that absorption and bolometric corrections increase ~exponentially with decrease of the color temperature, therefore the softest sources are truly luminous.

Thus, we classify sources to the left of the red line in Fig.5 as classical super-soft X-ray sources. We also include those sources which are located outside the stable nuclear burning boundary but their error bars cross this boundary. In addition, we added to this list two sources in M101, located outside but close to the stable nuclear burning boundary (the two sources in Fig.5 upper right panel with $kT \gtrsim 100$ eV and $L_X \gtrsim 10^{37}$ erg/s.). The catalog of super-soft X-ray sources in presented in Table C.1, and their numbers in galaxies from our sample are listed in Table 2.

6.2. Specific frequency of super-soft X-ray sources across morphological types

From Fig.5, it is evident that super-soft X-ray sources are considerably more abundant in late-type galaxies than in early-type galaxies. However, for a statistically sound conclusion one needs to take into consideration completeness limits of various data sets. To this end we used the sensitivity limit for M51 galaxy, corrected for the difference in the absorption column density as described in Section 5.2, to select super-soft X-ray sources. In each galaxy, we selected sources to the left of the thick red line and above the dashed blue line in Fig. 5. This selection is within the 20 counts flux limit (solid black line in Fig. 5.) in all galaxies, except for M83, where at the low temperature end, the 20 counts limit

for this galaxy is by a factor of about ~ 2 higher. This may result to slight underestimation of the specific frequency of super-soft sources in late-type galaxies. In counting super-soft sources, we included all the sources which error bars crossed the stable nuclear burning boundary. We also included two sources in M101, located outside but close to the stable nuclear burning boundary (the two sources in Fig.5 upper right panel with $kT \gtrsim 100$ eV and $L_X \gtrsim 10^{37}$ erg/s). In Centaurus A galaxy, we used different criteria for sources locate in and outside the dust lanes (c.f. dotted line in Fig. 5), although this does not change the final result.

In order to estimate specific frequencies of super-soft X-ray sources, we group the data separately for early- and late-type galaxies. There are 29 super-soft sources in late-type galaxies (M83, M51, M81, M101), which, for the total stellar mass of 13.9×10^{10} $M_\odot$ yield the specific frequency of

$$f^{\rm S}_{\rm SSS} \approx (2.08 \pm 0.46) \times 10^{-10}\ M_\odot^{-1} \tag{9}$$

In computing statistical errors we used Gehrels approximation (Gehrels 1986). Counting lenticular and elliptical galaxies together (Centaurus A, NGC3115, NGC3379, NGC4278, NGC4697), we find 7 super-soft X-ray sources sources for the total stellar mass of 28.3×10^{10} $M_\odot$ yielding specific frequency of

$$f^{\rm E+S0}_{\rm SSS} \approx (2.47 \pm 1.34) \times 10^{-11} M_\odot^{-1} \tag{10}$$

Centaurus A galaxy, although classified as S0, shows some star-formation activity within its dust lanes, at the the level of ~ 0.8 $M_\odot$/yr (Espada et al. 2019). However, its SSS specific frequency is closer to early-type galaxies than to late-type galaxies. In order to check how its inclusion in our sample affects our results, we compute SSS specific frequency for elliptical galaxies only:

$$f^{\rm E}_{\rm SSS} \approx (2.02 \pm 1.38) \times 10^{-11} M_\odot^{-1} \tag{11}$$

This number is ~ 20% smaller but compatible with the value obtained including Centaurus A.

The lower limit for the SSS specific frequency in early-type galaxies at the 3σ confidence level is $f^{\rm E}_{\rm SSS} > 8.2 \times 10^{-12} M_\odot^{-1}$.

The ratio of specific frequencies of SSS in late-type to early-type galaxies is

$$f^{\rm E+S0}_{\rm SSS}/f^{\rm S}_{\rm SSS} = 0.12 \pm 0.05 \tag{12}$$

i.e. late-type galaxies contain about ≈ 8 times more super-soft X-ray sources than early-type galaxies. Using Bayesian approach, we estimate that their specific frequencies are different at the confidence level corresponding to about ≈ 5.8σ.

We searched for variations of the SSS specific frequency between galaxies of the same morphological type. To this end we compared observed numbers of super-soft X-ray sources in each galaxy with their expected values computed from the corresponding SSS specific frequency and stellar mass of the galaxy. For early-type galaxies we found no statistically significant deviations of observed numbers of super-soft X-ray sources from their expected values. This is not surprising, given small numbers of SSS in early-type galaxies. For the late-type galaxies, however, we observe statistically significant deviations in M83 and M81 where the observed numbers of super-soft sources differ from the expected values at the statistically significant levels exceeding ~ 3σ. This can be understood considering that populations of accreting nuclear burning white dwarfs are determined by the long-term star-formation history of the galaxy, rather than by its mass, as discussed in the following section.

For late-type galaxies, we also compute the SSS specific frequency per unit star formation rate. Using SFR values, collected from the literature (Table 1 and references there) we obtain:

$$f^{\rm S}_{\rm SSS} \approx (3.13 \pm 0.70)\ \ (M_\odot/yr)^{-1} \tag{13}$$

Overall, the numbers of super-soft X-ray sources in late-type galaxies appear to somewhat better correlate with their star-formation rate than with the stellar mass.

6.3. Comparison with previous work and discussion

The fact that super-soft X-ray sources tend to be predominantly associated with young stellar populations has been noted previously (e.g. Di Stefano & Kong 2004). Studying populations of soft sources in nearby galaxies, Di Stefano (2010) mentioned the difference in the numbers of soft sources in early- and late-type galaxies, however they did not quantify these trends. Bogdán & Gilfanov (2011) using sample of 12 nearby late-type galaxies concluded that specific frequencies (per unit K-band luminosity) of luminous, $L_X > 10^{36}$ erg/s, super-soft sources in disks of spiral galaxies by factor of ~2 exceed that of bulges. Taking into account that the typical M_*/L_K ratio for bulges are approximately twice larger than for disks, this translates to about 4 times difference in specific frequency per unit mass, i.e. shows qualitatively same trend as our comparison of late-type and early-type galaxies, although the particular numbers are different. The difference is due to the fact, that Bogdán & Gilfanov (2011) used a selection procedure to identify super-soft X-ray sources, based on the hardness ratio with the threshold, corresponding to kT=200 eV.

Population synthesis calculations of nuclear burning accreting WDs predict difference of specific frequencies of SSSs in spiral and elliptical galaxies (Chen et al. 2015). Using their model `a025qc17` we estimate specific frequencies of super-soft X-ray sources with X-ray luminosities exceeding 10^{36} erg/s. For spiral galaxies they obtained specific frequencies ranging from 4×10^{-10} to 2×10^{-9} sources per $M_\odot$, corresponding to absorption column densities of 3×10^{21} cm^{-2} and 3×10^{20} cm^{-2}. For elliptical galaxies they obtained ≈ 6×10^{-11} sources per $M_\odot$ (for column density 3×10^{20} cm^{-2}), i.e. ≳ 7 times less frequent that in late-type galaxies. The contrast between late- and early- type galaxies is well consistent with our observations, especially taking into account dependence of these numbers on the age of the host galaxy (Chen et al. 2015). However, the actual numbers of specific frequencies are by at least a factor off ~ 2 − 3 larger in simulations than in our data. Among other reasons, this can be understood as a result of an approximate account for absorption, as the numbers of observable super-soft X-ray sources are highly sensitive to the column density.

Another interesting result of this work is that within the morphological types, the number of super-soft X-ray sources does not seem to obey simple scaling relations with parameters of the host galaxy. In particular, there are large and statistically significant excursions in the specific frequency of SSS in spiral galaxies, normalised to their stellar

mass. This can be expected in the view of the results of WD population modelling which predict that the population of super-soft sources peaks at about 1 Gyr after the star formation event (Chen et al. 2015). For this reason, numbers of super-soft sources in galaxies should not be expected to scale with stellar-mass or current star-formation rate. In the more general context, low specific frequency of super-soft X-ray sources, especially in early-type galaxies, support earlier conclusion that they are not the major class of type Ia supernova progenitors (Di Stefano 2010; Gilfanov & Bogdán 2010; Johansson et al. 2014; Woods & Gilfanov 2014).

6.4. Other soft X-ray sources

Along with rare super-soft X-ray sources, in all galaxies from our sample there are much more abundant populations of soft sources with somewhat harder, but still soft, spectra, located to the right of the stable nuclear burning boundary in Fig. 5. These sources were previously classified as quasi-soft X-ray sources (Di Stefano & Kong 2004; Orio 2006). Among other hypothesis, it was proposed that they are associated with supernova remnants or with accreting black holes in the soft spectral state (e.g. Di Stefano & Kong 2004; Patel et al. 2013; Long et al. 2014; Kuntz et al. 2016), although the contribution of the latter should be minimal (Section 5.2)

The X-ray emitting SNRs will be largely unresolved by Chandra and appear as point sources. Indeed, the SNR emission shifts outside X-ray band when the shock slows down to about ~ 200 km/sec and the post-shock temperature drops below $\sim 10^6$ K (Vink 2017). This happens about $\sim 2 \times 10^4$ years after the explosion when the remnant size typically reaches $\sim 10-20$ pc (Blondin et al. 1998). At the distances of spiral galaxies 3.6~7.6 Mpc, linear dimension of $10-20$ pc corresponds to the angular size of $\sim 0.4-0.9''$, which can be barely resolved with Chandra ACIS for the brightest sources. Furthermore, the majority of supernova remnants will be classified by hardness ratio and median energy as soft sources.

To clarify the nature of soft sources, located to the right from the stable nuclear burning boundary, we used M83 as a test case. It is a galaxy with one of the best studied X-ray SNR population. Long et al. (2014) identified 87 X-ray detected SNR candidates based on their X-ray spectral properties, associations with optical emission nebulae and/or radio sources. From this sample, SNR nature of 67 sources was confirmed with optical spectroscopy using [SII]/Hα line ratio (Winkler et al. 2017). The list of 87 X-ray detected SNRs from Long et al. (2014) was cross-correlated with our catalog of X-ray sources detected in M83. With $1''$ matching radius, we found 66 matches, of which 6 sources have statistically significant emission beyond 2 keV and remaining 60 sources were classified as soft sources in our analysis. We replot $kT_{\rm bb} - L_X$ diagramm for M83 in Fig. 6 marking confirmed SNRs by cyan symbols. As one can see, all confirmed SNRs are located outside the stable hydrogen nuclear burning boundary on $kT_{\rm bb} - L_{\rm X}$ diagram (i.e. to the right of the thick red line in Fig. 6) and their distribution on the $kT_{\rm bb} - L_X$ plane is morphologically quite similar to the distribution of the bulk of quasi-soft sources. We therefore conclude that the majority of quasi-soft sources must be SNRs.

For many of the brightest quasi-soft sources in spiral galaxies likelihood values obtained in spectral fitting suggest that the spectrum is more complicated than predicted by a featureless black body model. A more detailed investigation of several such sources revealed that these deviations are mostly associated with the presence of emission lines in their spectra. In majority of cases the spectrum of thermal emission of optically thin plasma or a non-equilibrium ionization model significantly improved the quality of the fit, suggesting that these sources may be SNRs. However, such a detailed analysis is only possible for a handful of brightest sources.

In order to compare spectral properties of soft and super-soft sources, we combined their spectra in late- and early- type galaxies. Combined spectra are shown in Fig.7 separately for sources located inside and outside the stable hydrogen nuclear burning boundary on the $kT_{bb} - L_X$ diagram (see Section 5.2). For comparison, we also show the combined spectrum of confirmed SNRs in M83. As one can see, combined spectrum of soft sources in spiral galaxies shows strong Mg and S lines and matches very well the combined spectrum of SNRs in M83. Similar values of the equivalent width of Mg and S lines support our conclusion that the vast majority of soft sources in these galaxies must be supernova remnants. In early-type galaxies, on the contrary, combined spectrum of soft sources is harder and does not show strong emission lines. As it was discussed in Section 5.2, by the method of selection, soft sources in early-type galaxies should include large numbers of X-ray binaries and background AGN. On the other hand, super-soft sources in all galaxies have much softer spectra, as expected. Their spectra are broadly similar in late- and early-type galaxies, although the quality of the latter does not permit to make a more quantitative conclusion.

We finally note that the numbers and specific frequencies of soft sources in galaxies from our sample seem to follow same trend as super-soft sources, decreasing from late-type to early-type galaxies. However a detailed investigation of dependence of the specific frequency of SNRs on the morphological type would require a more accurate selection of sources and is outside the scope of the present paper.

7. Summary

Based on public *Chandra* archival data, we studied populations of soft and super-soft X-ray sources with the goal to investigate populations of stable nuclear burning accreting WDs.

To this end, we searched Chandra data archive and constructed a sample of galaxies optimal for studying populations of steady nuclear burning accreting white dwarfs. We aimed at constructing the best possible sample of such galaxies. We thus selected four late-type and five early-type galaxies with stellar masses $\gtrsim 10^{10}$ $M_\odot$ and Chandra X-ray sensitivity limits comparable or better than $\sim 10^{36}$ ergs/s. Our selection presents the nearly full sample of galaxies available in Chandra archive up to cycle 20, suitable for such a study (among galaxies fitting within the field of view of Chandra observation)

We proposed a new approach to identify population of soft and super-soft X-ray sources based on combination of hardness ratio and median energy. Distributions of sources

over median energy in late-type galaxies shows clear bimodality with a distinct populations of soft and super-soft sources. These sources show a rather compact distributions in the X-ray luminosity–temperature plane with temperatures of 20–300 eV and X-ray luminosities in the 10^{36}~10^{38} ergs/s range. The picture is more complex in lenticular and elliptical galaxies, where populations of soft sources smoothly connect to the populations of X-ray binaries and background AGN in their median energy distributions. For these galaxies we mainly used the lack of emission above 2 keV to select soft sources for detailed analysis.

We used X-ray luminosity–temperature diagram to further classify selected sources into super-soft and soft. To this end we used the boundary of stable hydrogen nuclear burning to separate super-soft X-ray sources – candidates to nuclear burning white dwarfs from the rest of the population of soft sources. In late-type galaxies, we found 29 super-soft source which yields the specific frequency of $f^{\rm S}_{\rm SSS}$≈(2.08±0.46)×10^{-10} $M_\odot^{-1}$. In lenticular and elliptical galaxies, there are 7 super-soft sources with the specific frequency of $f^{\rm E+S0}_{\rm SSS}$≈ (2.47±1.34)×10^{-11} $M_\odot^{-1}$. Specific frequencies in late-type and early-type galaxies differ at the statistical confidence of ≈ 5.8σ. The ratio of specific frequencies of super-soft X-ray sources in late-type galaxies and early-type galaxies is $f^{\rm E+S0}_{\rm SSS}/f^{\rm S}_{\rm SSS} = 0.12 \pm 0.05$. Our results are broadly consistent with the population synthesis modelling of the populations of stable nuclear burning accreting WDs.

8. Acknowledgements

This research has made use of data obtained from the Chandra Data Archive and software provided by the Chandra X-ray Center (CXC) in the application packages CIAO. This publication makes use of data products from the HyperLeda and RC3 database. This publication makes use of data products from the Two Micron All Sky Survey, which is a joint project of the University of Massachusetts and the Infrared Processing and Analysis Center/California Institute of Technology, funded by the National Aeronautics and Space Administration and the National Science Foundation; the NASA/IPAC Extragalactic Database (NED), which is operated by the Jet Propulsion Laboratory, California Institute of Technology, under contract with the National Aeronautics and Space Administration. The authors acknowledge partial support of this work by the Russian Government Program of Competitive Growth of Kazan Federal University (IG) and by the RSF grant 19-12-00369 (MG). The authors thank the anonymous referee for useful and inspiring suggestions which helped to improve the manuscript.

References

Arnaud, K. A. 1996, in Astronomical Society of the Pacific Conference Series, Vol. 101, Astronomical Data Analysis Software and Systems V, ed. G. H. Jacoby & J. Barnes, 17
Bell, E. F. & de Jong, R. S. 2001, ApJ, 550, 212
Blondin, J. M., Wright, E. B., Borkowski, K. J., & Reynolds, S. P. 1998, ApJ, 500, 342
Bogdán, Á. & Gilfanov, M. 2011, MNRAS, 412, 401
Bresolin, F., Ryan-Weber, E., Kennicutt, R. C., & Goddard, Q. 2009, ApJ, 695, 580
Cash, W. 1979, ApJ, 228, 939
Chen, H.-L., Woods, T. E., Yungelson, L. R., Gilfanov, M., & Han, Z. 2014, MNRAS, 445, 1912
Chen, H.-L., Woods, T. E., Yungelson, L. R., Gilfanov, M., & Han, Z. 2015, MNRAS, 453, 3024
Chen, H.-L., Woods, T. E., Yungelson, L. R., Gilfanov, M., & Han, Z. 2016, MNRAS, 458, 2916
Ciardullo, R., Feldmeier, J. J., Jacoby, G. H., et al. 2002, ApJ, 577, 31
Colombo, D., Meidt, S. E., Schinnerer, E., et al. 2014, ApJ, 784, 4
Cowley, A. P., Schmidtke, P. C., Crampton, D., & Hutchings, J. B. 1990, ApJ, 350, 288
Crosthwaite, L. P., Turner, J. L., Buchholz, L., Ho, P. T. P., & Martin, R. N. 2002, AJ, 123, 1892
Dame, T. M., Hartmann, D., & Thaddeus, P. 2001, ApJ, 547, 792
de Vaucouleurs, G., de Vaucouleurs, A., Corwin, Herold G., J., et al. 1991, Third Reference Catalogue of Bright Galaxies
Di Stefano, R. 2010, ApJ, 712, 728
Di Stefano, R. & Kong, A. K. H. 2003, ApJ, 592, 884
Di Stefano, R. & Kong, A. K. H. 2004, ApJ, 609, 710
Ebisawa, K., Mitsuda, K., & Hanawa, T. 1991, ApJ, 367, 213
Espada, D., Verley, S., Miura, R. E., et al. 2019, ApJ, 887, 88
Ferrarese, L., Mould, J. R., Stetson, P. B., et al. 2007, ApJ, 654, 186
Freedman, W. L., Madore, B. F., Gibson, B. K., et al. 2001, ApJ, 553, 47
Fruscione, A., McDowell, J. C., Allen, G. E., et al. 2006, in Society of Photo-Optical Instrumentation Engineers (SPIE) Conference Series, Vol. 6270, Society of Photo-Optical Instrumentation Engineers (SPIE) Conference Series, ed. D. R. Silva & R. E. Doxsey, 62701V
Gaia Collaboration, Brown, A. G. A., Vallenari, A., et al. 2018, A&A, 616, A1
Gaia Collaboration, Prusti, T., de Bruijne, J. H. J., et al. 2016, A&A, 595, A1
Garcia-Burillo, S., Guelin, M., & Cernicharo, J. 1993, A&A, 274, 123
Gehrels, N. 1986, ApJ, 303, 336
Gilfanov, M. & Bogdán, Á. 2010, Nature, 463, 924
Greiner, J. 1996, Catalog of Luminous Supersoft X-Ray Sources, ed. J. Greiner, Vol. 472, 299
Greiner, J., Hasinger, G., & Kahabka, P. 1991, A&A, 246, L17
Guelin, M., Zylka, R., Mezger, P. G., Haslam, C. G. T., & Kreysa, E. 1995, A&A, 298, L29
Henze, M., Pietsch, W., Haberl, F., et al. 2014, A&A, 563, A2
Henze, M., Pietsch, W., Haberl, F., et al. 2010, A&A, 523, A89
Henze, M., Pietsch, W., Haberl, F., et al. 2011, A&A, 533, A52
HI4PI Collaboration, Ben Bekhti, N., Flöer, L., et al. 2016, A&A, 594, A116
Hillman, Y., Prialnik, D., Kovetz, A., & Shara, M. M. 2015, MNRAS, 446, 1924
Ho, L. C., Li, Z.-Y., Barth, A. J., Seigar, M. S., & Peng, C. Y. 2011, ApJS, 197, 21
Hong, J., Schlegel, E. M., & Grindlay, J. E. 2004, ApJ, 614, 508
Hu, N., Wang, E., Lin, Z., et al. 2018, ApJ, 854, 68
Jarrett, T. H., Chester, T., Cutri, R., Schneider, S. E., & Huchra, J. P. 2003, AJ, 125, 525
Jarrett, T. H., Masci, F., Tsai, C. W., et al. 2013, AJ, 145, 6
Johansson, J., Woods, T. E., Gilfanov, M., et al. 2014, MNRAS, 442, 1079
Kahabka, P., Pietsch, W., & Hasinger, G. 1994, A&A, 288, 538
Kahabka, P. & Trumper, J. 1996, in Compact Stars in Binaries, ed. J. van Paradijs, E. P. J. van den Heuvel, & E. Kuulkers, Vol. 165, 425
Karachentsev, I. D., Makarov, D. I., & Kaisina, E. I. 2013, AJ, 145, 101
Kuntz, K. D., Long, K. S., & Kilgard, R. E. 2016, ApJ, 827, 46
Leroy, A. K., Walter, F., Bigiel, F., et al. 2009, AJ, 137, 4670
Long, K. S., Helfand, D. J., & Grabelsky, D. A. 1981, ApJ, 248, 925
Long, K. S., Kuntz, K. D., Blair, W. P., et al. 2014, ApJS, 212, 21
Makarov, D., Prugniel, P., Terekhova, N., Courtois, H., & Vauglin, I. 2014, A&A, 570, A13
Moustakas, J., Kennicutt, Robert C., J., Tremonti, C. A., et al. 2010, ApJS, 190, 233
Nomoto, K. 1982, ApJ, 253, 798
Nomoto, K., Saio, H., Kato, M., & Hachisu, I. 2007, ApJ, 663, 1269
Orio, M. 2006, ApJ, 643, 844
Pakull, M. W., Beuermann, K., van der Klis, M., & van Paradijs, J. 1988, A&A, 203, L27
Panei, J. A., Althaus, L. G., & Benvenuto, O. G. 2000, A&A, 353, 970
Patel, B., Di Stefano, R., Nelson, T., et al. 2013, ApJ, 771, 6
Paxton, B., Bildsten, L., Dotter, A., et al. 2011, ApJS, 192, 3
Paxton, B., Cantiello, M., Arras, P., et al. 2013, ApJS, 208, 4
Peletier, R. F., Davies, R. L., Illingworth, G. D., Davis, L. E., & Cawson, M. 1990, AJ, 100, 1091

Pietsch, W., Fliri, J., Freyberg, M. J., et al. 2005, A&A, 442, 879
Prestwich, A. H., Irwin, J. A., Kilgard, R. E., et al. 2003, ApJ, 595, 719
Prialnik, D. & Kovetz, A. 1995, ApJ, 445, 789
Rider, P. R. 1960, Journal of the American Statistical Association, 55, 148
Saha, A., Thim, F., Tammann, G. A., Reindl, B., & Sandage, A. 2006, ApJS, 165, 108
Serra, P., Oosterloo, T., Morganti, R., et al. 2012, MNRAS, 422, 1835
Smale, A. P., Corbet, R. H. D., Charles, P. A., et al. 1988, MNRAS, 233, 51
Soraisam, M. D., Gilfanov, M., Wolf, W. M., & Bildsten, L. 2016, MNRAS, 455, 668
Stanghellini, L., Magrini, L., Casasola, V., & Villaver, E. 2014, A&A, 567, A88
Starrfield, S., Timmes, F. X., Hix, W. R., et al. 2013, in Binary Paths to Type Ia Supernovae Explosions, ed. R. Di Stefano, M. Orio, & M. Moe, Vol. 281, 166–171
Strong, A. W. & Mattox, J. R. 1996, A&A, 308, L21
Struve, C., Oosterloo, T. A., Morganti, R., & Saripalli, L. 2010, A&A, 515, A67
Swartz, D. A., Ghosh, K. K., Suleimanov, V., Tennant, A. F., & Wu, K. 2002, ApJ, 574, 382
Taylor, M. B. 2006, in Astronomical Society of the Pacific Conference Series, Vol. 351, Astronomical Data Analysis Software and Systems XV, ed. C. Gabriel, C. Arviset, D. Ponz, & S. Enrique, 666
Tonry, J. L., Dressler, A., Blakeslee, J. P., et al. 2001, ApJ, 546, 681
Trümper, J., Hasinger, G., Aschenbach, B., et al. 1991, Nature, 349, 579
Truran, J. W. & Glasner, S. A. 1995, On the Nature of the Soft X-Ray Emission from Nova GQ Muscae 1983, ed. A. Bianchini, M. della Valle, & M. Orio, Vol. 205, 453
van den Heuvel, E. P. J., Bhattacharya, D., Nomoto, K., & Rappaport, S. A. 1992, A&A, 262, 97
Vink, J. 2017, X-Ray Emission Properties of Supernova Remnants, ed. A. W. Alsabti & P. Murdin, 2063
Voss, R. & Gilfanov, M. 2006, A&A, 447, 71
Walter, F., Brinks, E., de Blok, W. J. G., et al. 2008, AJ, 136, 2563
Weisskopf, M. C., Wu, K., Trimble, V., et al. 2007, ApJ, 657, 1026
Whelan, J. & Iben, Icko, J. 1973, ApJ, 186, 1007
Willmer, C. N. A. 2018, ApJS, 236, 47
Wilms, J., Allen, A., & McCray, R. 2000, ApJ, 542, 914
Winkler, P. F., Blair, W. P., & Long, K. S. 2017, ApJ, 839, 83
Wolf, W. M., Bildsten, L., Brooks, J., & Paxton, B. 2013, ApJ, 777, 136
Woods, T. E. & Gilfanov, M. 2013, MNRAS, 432, 1640
Woods, T. E. & Gilfanov, M. 2014, MNRAS, 439, 2351
Yaron, O., Prialnik, D., Shara, M. M., & Kovetz, A. 2005, ApJ, 623, 398
Yungelson, L. & Livio, M. 1998, ApJ, 497, 168
Yungelson, L. R. 2010, Astronomy Letters, 36, 780
Zhang, Z., Gilfanov, M., & Bogdán, Á. 2012, A&A, 546, A36

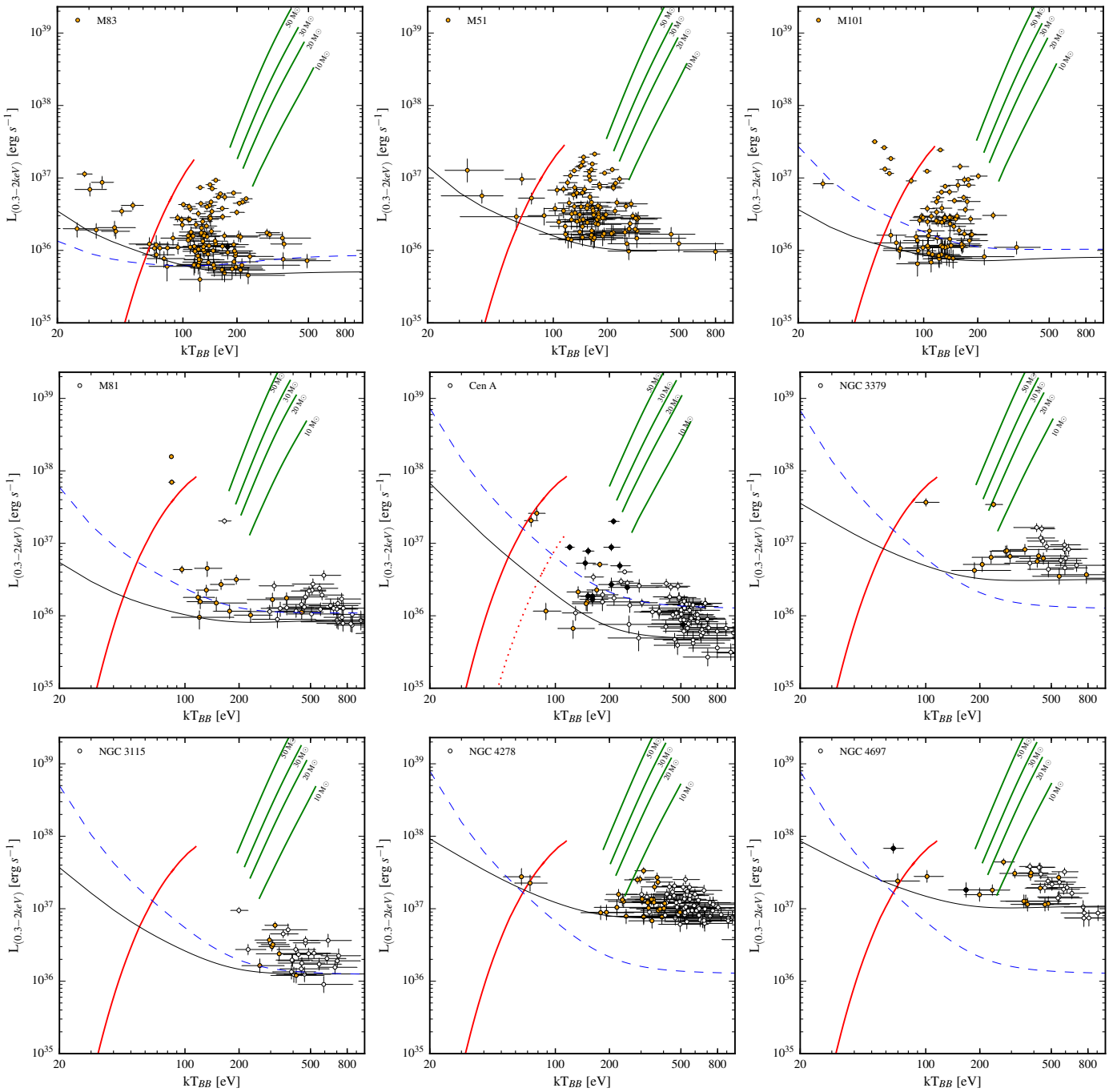

Fig. 5. The $kT_{\rm bb} - L_{\rm X}$ diagram of soft X-ray sources in galaxies from our sample. A cut of 20 net counts was applied. The luminosities are in the $0.3-2.0$ keV band and are not corrected for absorption. All plotted sources have no statistically significant flux above 2 keV (*open circles*). Sources with median energy $\tilde{E} \leq 1.2$ keV are shown with *solid orange circles*. Sources, having Gaia matches with measured parallax or proper motion are marked by *black diamonds*. *Solid red curves* show $kT_{bb} - L_X$ relations at the lower boundary of stable nuclear burning. Along these curves, the WD mass increases from $0.51M_\odot$ at the low-left end to $1.34M_\odot$ at the upper right end. The dotted red line for Centaurus A shows location of this boundary in the dust lanes of this galaxy. *Green lines* correspond to the emission spectrum of general relativistic accretion disk model around a Schwarzschild black hole (Ebisawa et al. 1991) for BH masses of 10, 20, 30 and $50M_\odot$. The accretion rate changes along the curves from $0.02\dot{M}_{\rm Edd}$ to $\dot{M}_{\rm Edd}$. Horizontally oriented *solid black* curves show the luminosity, corresponding to 20 net counts. *Dashed blue line* on each plot shows the 20 counts luminosity limit for M51 corrected for the difference in absorption column density between M51 and the galaxy under consideration. All model curves show absorbed luminosities. Errors are at 1σ confidence. See Section 5.2 for details of calculations.

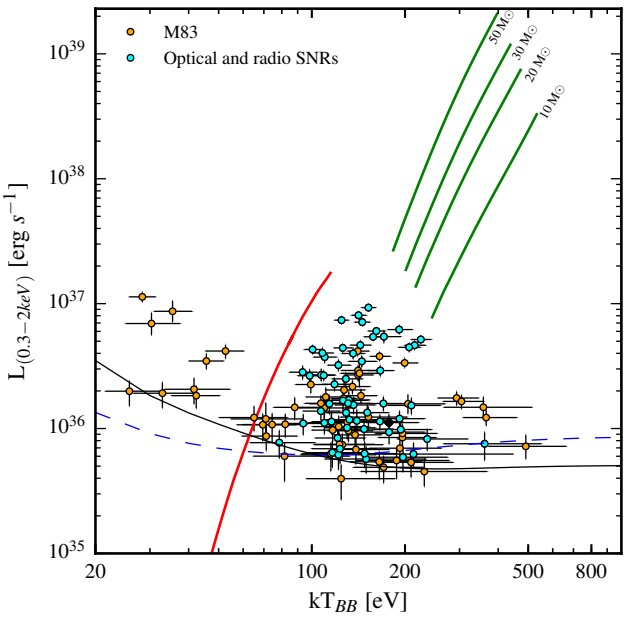

Fig. 6. The $kT_{\rm bb} - L_{\rm X}$ diagram of soft X-ray sources in M83. Supernova remnants confirmed by optical and radio data are shown by cyan circles. See caption to Fig. 5 for detailed description of $kT_{\rm bb} - L_{\rm X}$ diagram.

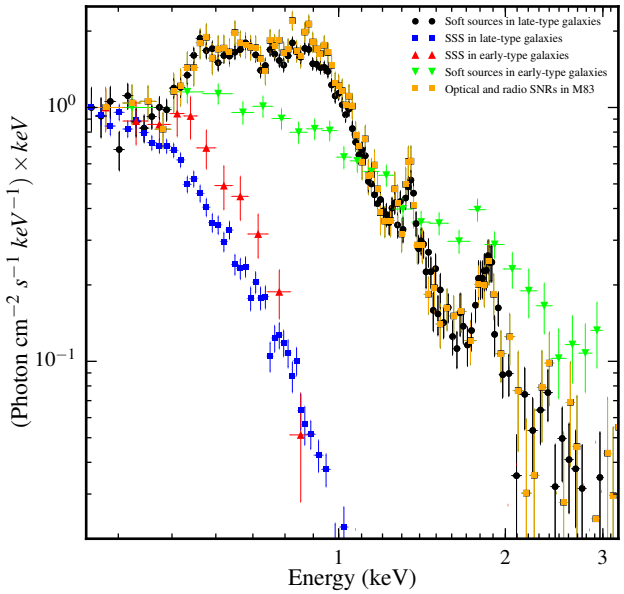

Fig. 7. Combined spectra of soft and super-soft X-ray sources in late- and early-type galaxies. *Black and green symbols* show integrated spectrum of all soft sources located outside the stable nuclear burning region for WDs (i.e. located to the right of the thick red line in Fig.5) in late- and early-type galaxies. *Yellow symbols* show integrated spectrum of sources, matching confirmed SNRs in M83. *Blue and red symbols* show the integrated spectra of super-soft X-ray sources, i.e. sources located to the left of and above the stable nuclear burning boundary in late-type and early-type galaxies respectively. The spectra are normalized to the same flux at 0.35 keV. See Section 6.1 for more detail.

Appendix A: List of observations

Table A.1 shows list of *Chandra* observations used in this paper. Columns are: (1) – Galaxy name; (2) – Observation identification number; (3) – Date of observations; (4) – Exposure time; (5) – Type of ACIS camera used during observations.

Appendix B: Galaxy images

Fig. B.1 shows X-ray images of galaxies in our sample and outlines of analysed regions.

Appendix C: Catalog of super-soft X-ray sources

The catalog is comprised of super-soft X-ray sources with more than 20 counts (solid black line in Fig. 5.) The sources are classified as super-soft if they are located to the left of the stable nuclear burning boundary (nearly vertical solid red line in n Fig. 5) or their error bars cross this boundary. We also included two sources in M101, located outside but close to the stable nuclear burning boundary (the two sources in Fig.5 upper right panel with $kT \gtrsim 100$ eV and $L_X \gtrsim 10^{37}$ erg/s.). The catalog of super-soft X-ray sources in given in Table C.1.

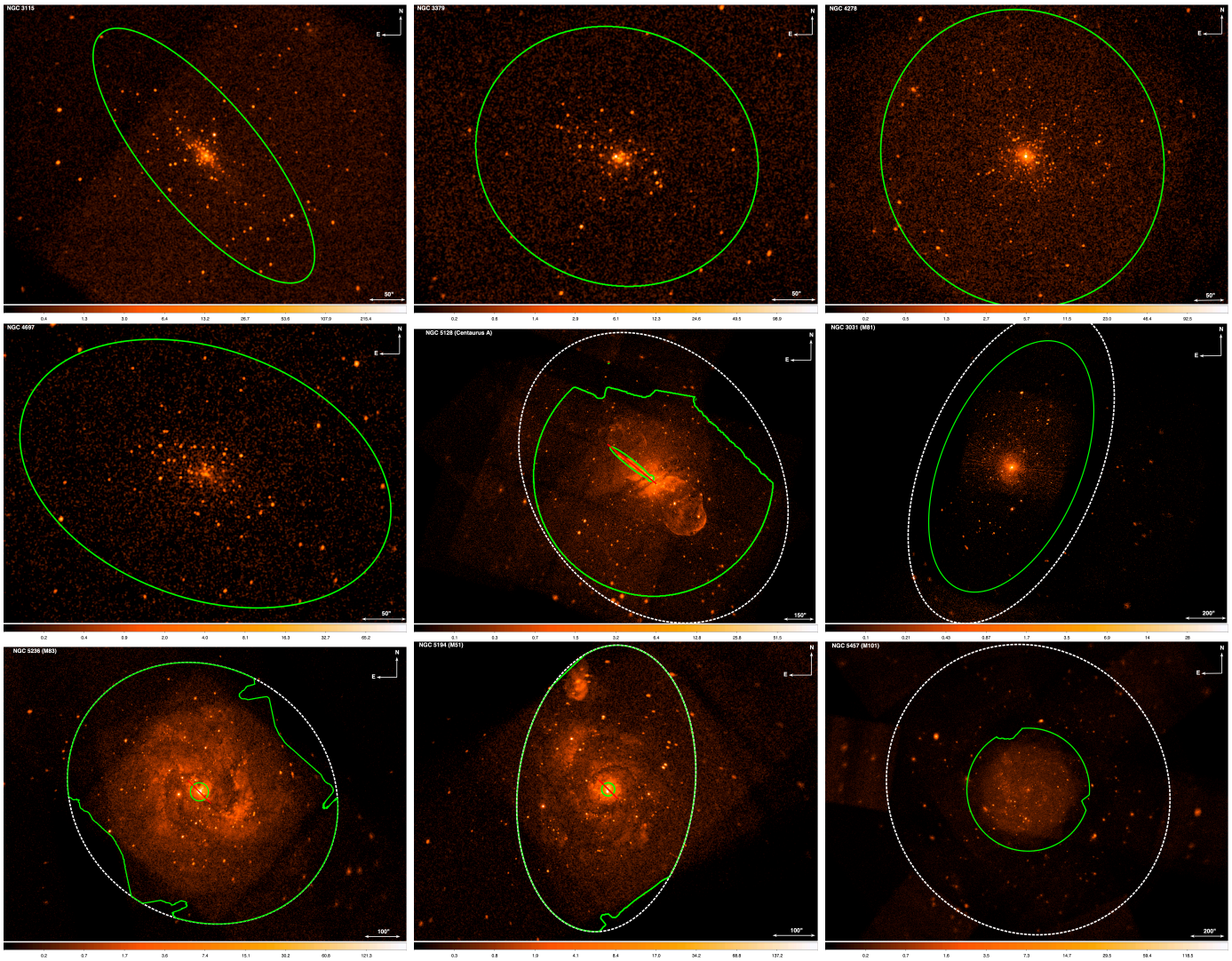

Fig. B.1. The 0.3–2 keV band false-color images (smoothed) of galaxies in our sample. Dashed white regions correspond to D_{25}. Green lines show regions used for source detection having exposure map values greater than 20 % of maximal value (for more detail see Section 3.1). Stellar masses listed in Table 2 are computed for these regions. The inside areas of small green regions near the center of Centaurus A, M83 and M51 were excluded from analysis.

Table A.1. List of *Chandra* observations used for the analysis.

Galaxy (1)	ObsID (2)	Date (3)	Exposure (ksec) (4)	Camera (5)
NGC 5236 (M83)	12992	04/09/2011	66.3	ACIS-S
	12993	15/03/2011	49.4	ACIS-S
	12994	23/03/2011	150.1	ACIS-S
	12995	23/12/2010	59.3	ACIS-S
	12996	29/03/2011	53.0	ACIS-S
	13202	25/12/2010	98.8	ACIS-S
	13241	18/03/2011	79.0	ACIS-S
	13248	18/03/2011	54.3	ACIS-S
	14332	29/08/2011	52.4	ACIS-S
	14342	28/12/2011	67.1	ACIS-S
NGC 5194 (M51)	13812	12/09/2012	157.5	ACIS-S
	13813	09/09/2012	179.2	ACIS-S
	13814	20/09/2012	189.8	ACIS-S
	13815	23/09/2012	67.2	ACIS-S
	13816	26/09/2012	73.1	ACIS-S
	15496	19/09/2012	41.0	ACIS-S
	15553	10/10/2012	37.6	ACIS-S
NGC 3031 (M81)	5935	26/05/2005	11.0	ACIS-S
	5936	28/05/2005	11.4	ACIS-S
	5937	01/06/2005	12.0	ACIS-S
	5938	03/06/2005	11.8	ACIS-S
	5939	06/062005	11.8	ACIS-S
	5940	09/06/2005	12.0	ACIS-S
	5941	11/06/2005	11.8	ACIS-S
	5942	15/06/2005	11.9	ACIS-S
	5943	18/06/2005	12.0	ACIS-S
	5944	21/06/2005	11.8	ACIS-S
	5945	24/06/2005	11.6	ACIS-S
	5946	26/06/2005	12.0	ACIS-S
	5947	29/06/2005	10.7	ACIS-S
	5948	03/07/2005	12.0	ACIS-S
	5949	06/07/2005	12.0	ACIS-S
NGC 5457 (M101)	4731	19/01/2004	56.2	ACIS-S
	4732	19/03/2004	69.8	ACIS-S
	4733	07/05/2004	24.8	ACIS-S
	4734	11/07/2004	35.5	ACIS-S
	4735	12/09/2004	28.8	ACIS-S
	4736	01/11/2004	77.3	ACIS-S
	4737	01/01/2005	21.9	ACIS-S
	5296	21/01/2004	3.1	ACIS-S
	5297	24/01/2004	21.7	ACIS-S
	5300	07/03/2004	52.1	ACIS-S
	5309	14/03/2004	70.8	ACIS-S
	5322	03/05/2004	64.7	ACIS-S
	5323	09/05/2004	42.6	ACIS-S
	5337	05/07/2004	9.9	ACIS-S
	5338	06/07/2004	28.6	ACIS-S
	5339	07/07/2004	14.3	ACIS-S
	5340	08/07/2004	54.4	ACIS-S
	6114	05/09/2004	66.2	ACIS-S
	6115	08/09/2004	35.8	ACIS-S
	6118	11/09/2004	11.5	ACIS-S
	6152	07/11/2004	44.1	ACIS-S
	6169	30/12/2004	29.4	ACIS-S
	6170	22/12/2004	48.0	ACIS-S
	6175	24/12/2004	40.7	ACIS-S
NGC 5128 (Cen A)	7797	22/03/2007	96.9	ACIS-I
	7798	27/03/2007	90.8	ACIS-I
	7799	30/03/2007	94.8	ACIS-I
	7800	17/04/2007	90.8	ACIS-I

	8489	08/05/2007	93.9	ACIS-I
	8490	30/05/2007	94.4	ACIS-I
NGC 3379	7073	23/01/2006	84.1	ACIS-S
	7074	09/04/2006	69.1	ACIS-S
	7075	07/03/2006	83.1	ACIS-S
	7076	10/01/2007	69.2	ACIS-S
NGC 3115	13817	18/01/2012	172.0	ACIS-S
	13819	26/01/2012	75.5	ACIS-S
	13820	31/01/2012	184.2	ACIS-S
	13821	03/02/2012	158.0	ACIS-S
	13822	21/01/2012	160.2	ACIS-S
	14383	04/04/2012	119.5	ACIS-S
	14384	06/04/2012	69.7	ACIS-S
	14419	05/04/2012	46.3	ACIS-S
NGC 4278	7077	16/03/2006	110.3	ACIS-S
	7078	25/07/2006	51.4	ACIS-S
	7079	24/10/2006	105.1	ACIS-S
	7080	20/04/2007	55.8	ACIS-S
	7081	20/02/2007	110.7	ACIS-S
NGC 4697	4727	26/12/2003	39.9	ACIS-S
	4728	06/01/2004	35.7	ACIS-S
	4729	12/02/2004	38.1	ACIS-S
	4730	18/08/2007	40.0	ACIS-S

Table C.1. List of super-soft X-ray sources.

ID	GALAXY	R.A.	DEC.	$Counts_{0.3-2}$	$Bkg_{0.3-2}$	$Rate_{0.3-2}$ (10^{-4} cnt/s)	N_H ($10^{21} cm^{-2}$)	kT_{bb} (eV)	$L_X^{0.3-2}$ (10^{37} erg/s)
(1)	(2)	(3)	(4)	(5)	(6)	(7)	(8)	(9)	(10)
1	M81	09 55 42.14	+69 03 36.40	2565.0 ± 51.7	8.7 ± 0.9	145.30 ± 2.94	1.19	85^{+2}_{-1}	$15.87^{+0.34}_{-0.32}$
2	M81	09 56 8.98	+69 01 6.79	360.0 ± 20.0	1.6 ± 0.5	20.37 ± 1.14	1.39	86^{+4}_{-3}	$7.04^{+0.48}_{-0.46}$
3	NGC3379	10 47 47.23	+12 34 59.78	72.0 ± 9.5	0.5 ± 0.3	3.03 ± 0.40	0.26	100^{+18}_{-13}	$3.68^{+0.46}_{-0.42}$
4	NGC4278	12 19 56.67	+29 16 31.08	20.0 ± 5.6	1.6 ± 0.5	0.42 ± 0.13	0.20	65^{+18}_{-13}	$2.76^{+0.82}_{-0.63}$
5	NGC4278	12 20 12.43	+29 17 41.86	25.0 ± 6.1	1.3 ± 0.4	0.55 ± 0.14	0.20	72^{+18}_{-13}	$2.26^{+0.64}_{-0.50}$
6	NGC4697	12 48 34.55	–5 47 49.34	36.0 ± 7.1	0.8 ± 0.3	2.29 ± 0.46	0.21	102^{+24}_{-15}	$2.79^{+0.58}_{-0.47}$
7	NGC4697	12 48 41.28	–5 48 19.73	24.0 ± 6.0	0.2 ± 0.2	1.55 ± 0.39	0.21	70^{+23}_{-12}	$2.41^{+0.63}_{-0.52}$
8	CenA	13 25 14.60	–42 56 11.57	83.0 ± 10.2	19.3 ± 1.4	2.28 ± 0.37	0.24	79^{+9}_{-8}	$2.60^{+0.56}_{-0.47}$
9	CenA	13 25 18.14	–43 03 42.53	100.0 ± 11.0	27.8 ± 1.7	1.29 ± 0.20	0.24	73^{+7}_{-6}	$2.06^{+0.43}_{-0.36}$
10	M51	13 29 41.23	+47 11 15.57	48.0 ± 8.0	16.1 ± 1.2	0.43 ± 0.11	0.92	33^{+20}_{-8}	$1.27^{+0.56}_{-0.39}$
11	M51	13 29 46.00	+47 10 56.36	55.0 ± 8.5	9.5 ± 1.0	0.61 ± 0.11	0.69	67^{+13}_{-13}	$0.96^{+0.19}_{-0.16}$
12	M51	13 29 51.69	+47 12 3.82	86.1 ± 10.3	56.9 ± 2.3	0.39 ± 0.14	3.93	62^{+28}_{-32}	$0.29^{+0.09}_{-0.10}$
13	M51	13 29 54.02	+47 11 25.68	64.0 ± 9.0	15.4 ± 1.2	0.65 ± 0.12	2.89	40^{+12}_{-16}	$0.57^{+0.12}_{-0.12}$
14	M51	13 29 54.99	+47 12 4.74	62.0 ± 8.9	16.0 ± 1.3	0.62 ± 0.12	2.92	76^{+14}_{-12}	$0.53^{+0.09}_{-0.09}$
15	M83	13 36 52.45	–29 52 52.09	242.0 ± 16.6	113.3 ± 3.2	1.76 ± 0.23	5.40	53^{+7}_{-8}	$0.42^{+0.05}_{-0.05}$
16	M83	13 36 52.66	–29 49 37.45	67.0 ± 9.2	9.1 ± 1.0	0.79 ± 0.13	1.32	35^{+4}_{-6}	$0.87^{+0.18}_{-0.15}$
17	M83	13 36 53.97	–29 50 32.52	40.0 ± 7.4	14.3 ± 1.2	0.35 ± 0.10	3.60	33^{+6}_{-9}	$0.19^{+0.04}_{-0.05}$
18	M83	13 36 56.45	–29 52 57.25	50.0 ± 8.1	21.3 ± 1.5	0.39 ± 0.11	5.00	26^{+4}_{-7}	$0.20^{+0.04}_{-0.05}$
19	M83	13 36 56.77	–29 53 16.20	95.0 ± 10.8	22.5 ± 1.5	0.99 ± 0.15	3.39	46^{+6}_{-6}	$0.35^{+0.05}_{-0.05}$
20	M83	13 36 58.62	–29 51 56.84	88.0 ± 10.4	49.2 ± 2.1	0.53 ± 0.15	10.41	74^{+15}_{-22}	$0.11^{+0.02}_{-0.03}$
21	M83	13 36 58.64	–29 53 38.86	87.0 ± 10.4	30.6 ± 1.7	0.77 ± 0.14	1.82	30^{+5}_{-7}	$0.69^{+0.15}_{-0.13}$
22	M83	13 36 59.04	–29 52 18.07	50.0 ± 8.1	22.5 ± 1.5	0.38 ± 0.11	11.69	71^{+12}_{-18}	$0.09^{+0.02}_{-0.02}$
23	M83	13 36 59.25	–29 51 43.82	85.0 ± 10.3	49.4 ± 2.2	0.49 ± 0.14	9.95	69^{+12}_{-20}	$0.11^{+0.02}_{-0.03}$
24	M83	13 36 59.34	–29 53 17.90	49.0 ± 8.1	19.1 ± 1.3	0.41 ± 0.11	2.50	65^{+15}_{-18}	$0.12^{+0.03}_{-0.03}$
25	M83	13 37 0.45	–29 50 54.02	173.0 ± 14.2	9.1 ± 1.0	2.25 ± 0.19	4.05	28^{+3}_{-3}	$1.13^{+0.10}_{-0.10}$
26	M83	13 37 3.86	–29 52 23.02	41.0 ± 7.5	10.8 ± 1.0	0.41 ± 0.10	4.36	42^{+7}_{-8}	$0.18^{+0.03}_{-0.04}$
27	M83	13 37 5.53	–29 50 32.24	34.0 ± 6.9	6.0 ± 0.8	0.42 ± 0.10	3.01	42^{+8}_{-13}	$0.21^{+0.05}_{-0.05}$
28	M83	13 37 18.55	–29 52 7.59	29.0 ± 6.5	10.6 ± 1.0	0.25 ± 0.09	1.57	71^{+16}_{-23}	$0.12^{+0.04}_{-0.03}$
29	M101	14 02 51.34	+54 19 18.24	178.0 ± 14.4	14.7 ± 1.2	2.02 ± 0.18	1.50	85^{+6}_{-5}	$0.91^{+0.08}_{-0.07}$
30	M101	14 02 51.64	+54 22 3.97	33.0 ± 6.8	10.5 ± 1.0	0.28 ± 0.08	1.17	70^{+24}_{-17}	$0.13^{+0.03}_{-0.03}$
31	M101	14 03 1.22	+54 23 41.41	324.0 ± 19.0	13.3 ± 1.1	3.83 ± 0.23	1.13	66^{+3}_{-3}	$1.85^{+0.12}_{-0.11}$
32	M101	14 03 12.75	+54 21 11.52	38.0 ± 7.2	13.1 ± 1.1	0.28 ± 0.08	1.99	73^{+18}_{-14}	$0.10^{+0.02}_{-0.02}$

33	M101	14 03 13.65	+54 20 9.39	700.0 ± 27.5	10.9 ± 1.0	7.24 ± 0.29	1.57	53^{+2}_{-2}	$3.17^{+0.13}_{-0.13}$
34	M101	14 03 15.52	+54 17 3.81	339.0 ± 19.4	30.7 ± 1.7	3.24 ± 0.20	2.52	104^{+5}_{-5}	$1.24^{+0.07}_{-0.07}$
35	M101	14 03 16.52	+54 20 54.80	44.0 ± 7.7	12.5 ± 1.1	0.34 ± 0.08	1.85	66^{+14}_{-11}	$0.16^{+0.03}_{-0.03}$
36	M101	14 03 19.02	+54 17 19.48	254.0 ± 17.0	33.5 ± 1.8	2.32 ± 0.18	1.40	61^{+4}_{-4}	$1.32^{+0.10}_{-0.09}$
37	M101	14 03 27.38	+54 21 11.62	109.0 ± 11.5	24.4 ± 1.5	0.89 ± 0.12	1.67	27^{+4}_{-3}	$0.83^{+0.12}_{-0.11}$
38	M101	14 03 29.91	+54 20 57.27	259.0 ± 17.1	16.7 ± 1.3	2.54 ± 0.18	1.81	64^{+4}_{-3}	$1.15^{+0.08}_{-0.08}$
39	M101	14 03 33.35	+54 17 59.73	433.0 ± 21.8	22.2 ± 1.4	4.32 ± 0.23	2.24	60^{+3}_{-2}	$2.62^{+0.14}_{-0.14}$

Description of columns: (1) Source ID; (2) Galaxy name; (3) Right ascension (J2000); (4) Declination (J2000); (5) Counts in the source region in the 0.3-2 keV band and its 1σ error; (6) Background counts in the source region in 0.3–2 keV band and its 1σ error (68%); (7) Source count rate in 0.3–2 keV band ; (8) Absorption column density in units of 10^{21} cm^{-2} obtained by combining CO 2-1 and 21 cm data as described in Section 5.1; (9) best fit color temperature in units of eV; (10) absorbed X-ray luminosity in the 0.3-2 keV band in units of 10^{37} erg s^{-1}. Parameters given in columns (9) and (10) were obtained by approximating spectra with the black body model with absorption fixed at the value from column (8).